

## On the Use of Field RR Lyrae as Galactic Probes. II. A new $\Delta S$ calibration to estimate their metallicity \*

J. CRESTANI,<sup>1,2,3</sup> M. FABRIZIO,<sup>2,4</sup> V. F. BRAGA,<sup>2,4</sup> C. SNEDEN,<sup>5</sup> G. PRESTON,<sup>6</sup> I. FERRARO,<sup>2</sup> G. IANNICOLA,<sup>2</sup> G. BONO,<sup>1,2</sup>  
A. ALVES-BRITO,<sup>3</sup> M. NONINO,<sup>7</sup> V. D'ORAZI,<sup>8,9</sup> L. INNO,<sup>10,11</sup> M. MONELLI,<sup>12</sup> J. STORM,<sup>13</sup> G. ALTAVILLA,<sup>2,4</sup>  
B. CHABOYER,<sup>14</sup> M. DALL'ORA,<sup>10</sup> G. FIORENTINO,<sup>2</sup> C. GILLIGAN,<sup>14</sup> E. K. GREBEL,<sup>15</sup> H. LALA,<sup>15</sup> B. LEMASLE,<sup>15</sup>  
M. MARENGO,<sup>16</sup> S. MARINONI,<sup>2,4</sup> P. M. MARRESE,<sup>2,4</sup> C. E. MARTÍNEZ-VÁZQUEZ,<sup>17</sup> N. MATSUNAGA,<sup>18</sup> J. P. MULLEN,<sup>16</sup>  
J. NEELEY,<sup>19</sup> Z. PRUDIL,<sup>15</sup> R. DA SILVA,<sup>2,4</sup> P. B. STETSON,<sup>20</sup> F. THÉVENIN,<sup>21</sup> E. VALENTI,<sup>22,23</sup> A. WALKER,<sup>17</sup> AND  
M. ZOCCALI<sup>24</sup>

<sup>1</sup>*Dipartimento di Fisica, Università di Roma Tor Vergata, via della Ricerca Scientifica 1, 00133 Roma, Italy*

<sup>2</sup>*INAF – Osservatorio Astronomico di Roma, via Frascati 33, 00078 Monte Porzio Catone, Italy*

<sup>3</sup>*Departamento de Astronomia, Universidade Federal do Rio Grande do Sul, Av. Bento Gonçalves 6500, Porto Alegre 91501-970, Brazil*

<sup>4</sup>*Space Science Data Center – ASI, via del Politecnico snc, 00133 Roma, Italy*

<sup>5</sup>*Department of Astronomy and McDonald Observatory, The University of Texas, Austin, TX 78712, USA*

<sup>6</sup>*The Observatories of the Carnegie Institution for Science, 813 Santa Barbara St., Pasadena, CA 91101, USA*

<sup>7</sup>*INAF – Osservatorio Astronomico di Trieste, Via G. B. Tiepolo 11, 34143 Trieste, Italy*

<sup>8</sup>*INAF – Osservatorio Astronomico di Padova, vicolo dell'Osservatorio 5, 35122, Padova, Italy*

<sup>9</sup>*School of Physics and Astronomy, Monash University, Clayton, VIC 3800, Melbourne, Australia*

<sup>10</sup>*INAF – Osservatorio Astronomico di Capodimonte, Salita Moiariello 16, 80131 Napoli, Italy*

<sup>11</sup>*Università Parthenope di Napoli, Science and Technology Department, CDN IC4, 80143 Naples, Italy*

<sup>12</sup>*Instituto de Astrofísica de Canarias, Calle Via Lactea s/n, E38205 La Laguna, Tenerife, Spain*

<sup>13</sup>*Leibniz-Institut für Astrophysik Potsdam (AIP), An der Sternwarte 16, D-14482 Potsdam, Germany*

<sup>14</sup>*Department of Physics and Astronomy, Dartmouth College, Hanover, NH 03784, USA*

<sup>15</sup>*Astronomisches Rechen-Institut, Zentrum für Astronomie der Universität Heidelberg, Mönchhofstr. 12-14, D-69120 Heidelberg, Germany*

<sup>16</sup>*Department of Physics and Astronomy, Iowa State University, Ames, IA 50011, USA*

<sup>17</sup>*Cerro Tololo Inter-American Observatory, NSF's National Optical-Infrared Astronomy Research Laboratory, Casilla 603, La Serena, Chile*

<sup>18</sup>*Department of Astronomy, The University of Tokyo, 7-3-1 Hongo, Bunkyo-ku, Tokyo 113-0033, Japan*

<sup>19</sup>*Department of Physics, Florida Atlantic University, 777 Glades Rd, Boca Raton, FL 33431 USA*

<sup>20</sup>*Herzberg Astronomy and Astrophysics, National Research Council, 5071 West Saanich Road, Victoria, British Columbia V9E 2E7, Canada*

<sup>21</sup>*Université de Nice Sophia-antipolis, CNRS, Observatoire de la Côte d'Azur, Laboratoire Lagrange, BP 4229, F-06304 Nice, France*

<sup>22</sup>*European Southern Observatory, Karl-Schwarzschild-Str. 2, 85748 Garching bei München, Germany*

<sup>23</sup>*Excellence Cluster ORIGINS, Boltzmann-Straße 2, D-85748 Garching bei München, Germany*

<sup>24</sup>*Instituto de Astrofísica, Facultad de Física, Pontificia Universidad Católica de Chile, Av. Vicuña Mackenna 4860, Santiago, Chile*

(Received September 30, 2020; Revised November 19, 2020; Accepted December 3, 2020)

Submitted to ApJ

ABSTRACT

Corresponding author: J. Crestani

juliana.crestani@uniroma1.it

\* Based on observations obtained with the du Pont telescope at Las Campanas Observatory, operated by Carnegie Institution for Science. Based in part on data collected at Subaru Telescope, which is operated by the National Astronomical Observatory of Japan. Based partly on data obtained with the STELLA robotic telescopes in Tenerife, an AIP facility jointly operated by AIP and IAC. Some of the observations reported in this paper were obtained with the Southern African Large Telescope (SALT). Based on observations made with the Italian Telescopio Nazionale Galileo (TNG) operated on the island of La Palma by the Fundación Galileo Galilei of the INAF (Istituto Nazionale di Astrofisica) at the Spanish Observatorio del Roque de los Muchachos of the Instituto de Astrofísica de Canarias. Based on observations collected at the European Organisation for Astronomical Research in the Southern Hemisphere.

We performed the largest and most homogeneous spectroscopic survey of field RR Lyraes (RRLs). We secured  $\approx 6,300$  high resolution (HR,  $R \sim 35,000$ ) spectra for 143 RRLs (111 fundamental, RRab; 32 first overtone, RRC). The atmospheric parameters were estimated by using the traditional approach and the iron abundances were measured by using an LTE line analysis. The resulting iron distribution shows a well defined metal-rich tail approaching solar iron abundance. This suggests that field RRLs experienced a complex chemical enrichment in the early halo formation. We used these data to develop a new calibration of the  $\Delta S$  method. This diagnostic, based on the equivalent widths of CaII K and three Balmer ( $H_{\delta, \gamma, \beta}$ ) lines, traces the metallicity of RRLs. For the first time the new empirical calibration: i) includes spectra collected over the entire pulsation cycle; ii) includes RRC variables; iii) relies on spectroscopic calibrators covering more than three dex in iron abundance; iv) provides independent calibrations based on one/two/three Balmer lines. The new calibrations were applied to a dataset of both SEGUE-SDSS and degraded HR spectra totalling 6,451 low resolution (LR,  $R \sim 2,000$ ) spectra for 5,001 RRLs (3,439 RRab, 1,562 RRC). This resulted in an iron distribution with a median<sup>a)</sup>  $\eta = -1.55 \pm 0.01$  and  $\sigma = 0.51$  dex, in good agreement with literature values. We also found that RRC are 0.10 dex more metal-poor than RRab variables, and have a distribution with a smoother metal-poor tail. This finding supports theoretical prescriptions suggesting a steady decrease in the RRC number when moving from metal-poor to metal-rich stellar environments.

*Keywords:* Stars: variables: RR Lyrae — Galaxy: halo — Techniques: spectroscopic

## 1. INTRODUCTION

The RR Lyrae (RRL) stars are radially pulsating, core helium burning stars. The fundamental mode and the first overtone pulsators are categorized as RRab and RRC, respectively, with the RRd being a small population of double mode pulsators. Being evolved low mass stars, they are ubiquitous in a variety of environments and cover a wide metallicity range ( $[Fe/H] \approx -2.5$  to solar). Interestingly, the RRL obey period-luminosity relations in near-infrared bands (e.g. Longmore et al. 1986; Bono et al. 2003; Braga et al. 2018; Bono et al. 2019). These relations make them ideal standard candles, like Cepheids, but with the unique characteristics of tracing necessarily old populations ( $\geq 10$  Gyr) and being very well studied (e.g. Marconi et al. 2015). Indeed, Classical Cepheids trace exclusively young populations, while Type II Cepheids are old but scarce and still poorly understood (Bono et al. 2020a).

The absolute visual magnitude metallicity relation (Sandage & Tammann 2006) and the period-luminosity relations of the RRLs have made them very popular distance indicators for decades. Field RRLs have also been the focus of several spectroscopic studies (e.g. Preston 1959; Butler et al. 1976, 1979; Saha 1985; Layden 1994, hereafter Layden94), aimed at investigating the early chemical enrichment of both the Halo and the Bulge together with their three-dimensional spatial structure.

The question that immediately arises is whether chemical abundance determinations for these stars are reliable across their whole pulsation cycle. After all, even though their short (0.2 to 1 day) periods make their light curves relatively easy to obtain, the resulting rapid atmospheric changes could make detailed chemical abundance investigations very difficult, in particular for fainter objects. In the past, this difficulty was two-fold: first, there was the challenge of observing the star for a sufficiently long time in order to obtain a high signal-to-noise ratio (SNR), but not for so long as to cause the smearing of spectral lines due to the varying velocity of the atmospheric layer where the line is formed. Second, it was unclear whether the measured atmospheric metallicity of the RRL remained constant across the pulsation cycle.

The first issue was solved by the development of larger telescopes and increased access to them. Even 2 meter class telescopes have great success in obtaining a good SNR in high dispersion spectrographs for the brighter targets. With 8 m class telescopes, exposures as short as a few minutes deliver high quality spectra for medium to bright targets, allowing a very detailed study of the atmospheric phenomena in these stars (Chadid et al. 2008; Gillet et al. 2016). As for the second issue, the breakthrough came with the works of For et al. (2011) for the RRab and Sneden et al. (2017) for the RRC, both of which demonstrated that the observed metallicity of RRL remain constant within uncertainties for the entire pulsation cycle. The same result has been found by Magurno et al. (2019) for a large sample of RRL in the  $\omega$  Centauri globular cluster.

<sup>a)</sup> We employ the letter  $\eta$  in this work to refer to the median values of whatever quantity is being discussed, e.g. the median of a distribution, the median of the residuals in consideration.

These developments confirmed that coherent chemical abundance results can be recovered during the whole pulsation cycle, thus opening the door for random phase observations. This efficient approach to observations caused a significant increase in the number of RRL with spectroscopic studies. Indeed, with the nonlinear effects caused by shockwaves being restricted to a narrow phase window, a series of observations of any given RRL can easily provide perfectly useable data. However, high resolution spectroscopy is still a resource-consuming endeavour. A single RRL is capable of constraining both chemical abundance and distance, yet a detailed study of a stellar population requires a large number of such observations. It is still unviable to acquire high dispersion spectra for objects beyond the Milky Way, or obtain and analyse a very large number of such spectra to perform detailed studies of the Galactic halo. Both stellar distance and sample size are strong constraints on the applicability of high resolution spectroscopy.

Originally, the  $\Delta S$  method consisted in deriving two spectral types for a given RRL, one only considering the Balmer series features ( $H_\beta$ ,  $H_\gamma$ ,  $H_\delta$ ), and one only the CaII K line. The difference in spectral type between these two indicators was then associated to a difference in metallicity (Preston 1959; Butler 1975). Following this working hypothesis, the studies of Freeman & Rodgers (1975), Suntzeff et al. (1991), and Layden (1994) demonstrated that the equivalent widths of the CaII K and three of the Balmer series features can also be associated to the metallicity of a given RRL without the use of the spectral type. These features are extremely strong and can be reliably measured at very low spectral resolutions. This means that, once a calibration using high dispersion spectroscopy is derived, low resolution measurements are enough to provide metallicity estimates. This equivalent width approach is the basis of the  $\Delta S$  method as it is discussed in the present work.

The  $\Delta S$  method is behind the majority of metallicity estimates of RRL stars in the literature directly, via its application to low resolution spectra, or indirectly, when its results are used to calibrate other metallicity indicators such as the Fourier parameter decomposition method. This low resolution spectroscopic metallicity indicator is a balanced approach between the precision of high resolution spectroscopy and the efficiency of photometry. Wallerstein et al. (2012) have adapted the  $\Delta S$  method to use the infrared CaII line at 8,498 Å covered by the *Gaia* spectrograph (Cropper et al. 2018). Another related method using the CaII K line and the Balmer series features was employed by Liu et al. (2020), using synthetic spectra matching instead of equivalent widths.

The calibration provided by Layden94 is widely used in the literature (Dambis et al. 2013), although later ones exist (e.g. Gratton et al. 2004). It was produced using 19 RRab stars at minimum light phases and applied a metallicity scale transformation based on seven globular clusters to provide values in the Zinn & West (1984) scale. In this work, we employed the largest and most homogeneous high resolution spectroscopic sample of field RRL stars ever used in the literature to provide a brand new calibration of  $\Delta S$  method across the entire pulsation cycle for both RRab and RRC stars, including in the metal-rich and metal-poor tails that were previously poorly sampled.

Our sample allows us to both determine the metallicities in high resolution in a homogeneous way, and the  $\Delta S$  measurements once the spectra were downgraded to low resolution. With this, this new calibration makes use of no metallicity scale transformations. As we have dozens of calibrating stars, anyone who wishes to perform new measurements in our system has several good reference targets to choose from. This means no equivalent width system transformations are necessary either. Moreover, we streamlined some features of the IDL code EWIMH<sup>1</sup>, one of several codes traditionally employed for the  $\Delta S$  measurements, to make full use of the much higher quality spectrographs currently in use. These changes are easy to implement in other codes for the same purpose.

This paper is organized as follows. In Sect. 2 we describe the spectroscopic datasets, and in Sect. 3 how they are organised into samples. In Sect. 4 we discuss the changes made to the definition of the  $\Delta S$  method and the changes on how the measurements are performed by the code. The calibration between the  $\Delta S$  index and [Fe/H] is provided in Sect. 5. In Sect. 6 we compare our results with the literature in both high and low resolution. Finally, the calibration is applied to a large sample of field RRLs including hundreds of RRC and one RRD in Sect. 7. A summary and final remarks are given in Sect. 8. Further discussion regarding the differences between the current calibration and Layden94, and phase considerations are presented in Appendix A.

## 2. SPECTROSCOPIC DATA SETS

To provide firm constraints on the metallicity distribution of the Galactic halo, we adopted the same photometric catalog built in F19, the first paper of this series. To take into account new optical RRL catalogs

<sup>1</sup>The code and documentation can be found at <http://physics.bgsu.edu/~layden/ASTRO/DATA/EXPORT/EWIMH/ewimh.htm>

and surveys that have been recently published the original photometric catalog was complemented with four new data set provided by Catalina (Drake et al. 2017), PANSTARRS (Sesar et al. 2017), ASA-SN (Jayasinghe et al. 2019) and DECam (Stringer et al. 2019). The selection criteria are the same discussed in F19. The new final photometric catalog includes  $\sim 179,000$  RRLs and was the starting point for collecting the spectroscopic dataset. A detailed description of the construction of this catalog is provided in a companion paper (Braga et al. 2020, in preparation).

### 2.1. High resolution spectroscopic data set

We have collected a sample of 6,631 spectra for 266 stars (173 RRab, 92 RRc, 1 RRD, Tab. 1) across the pulsation phase from multiple medium and high resolution spectrographs. The largest and most homogeneous subsample was collected with the echelle spectrograph at du Pont (Las Campanas Observatory) and includes 6,070 high resolution ( $R=35,000$ ) spectra of 186 RRL (107 RRab, 79 RRc). It typically covers wavelengths from 3,600 to 9,300 Å.

These data were complemented with 530 optical spectra from the ESO Archive. We included spectra from UVES and X-shooter at VLT (Cerro Paranal Observatory), HARPS at the 3.6m telescope (La Silla Observatory), and FEROS at the 2.2m telescope (La Silla Observatory). An additional 10 spectra were added from HARPS-N at the Telescopio Nazionale Galileo (Roque de Los Muchachos Observatory), 4 from HRS (Crause et al. 2014) at SALT (South African Astronomical Observatory), 6 from the HDS (Noguchi et al. 2002) at Subaru (National Astronomical Observatory of Japan) and 11 from the echelle spectrograph (Weber et al. 2012) at STELLA (Izana Observatory). Typical spectra for all spectrographs can be seen in Fig. 1.

The distribution of exposure times peaks at  $\approx 400$  seconds, with an average 434 seconds, and standard deviation 303 seconds. The reddening- and distance-independent photometric characteristics of the  $\Delta S$  calibrating sample, discussed in greater detail in Sect. 3, are shown in Fig. 2. Visual magnitudes and amplitudes were derived from *Gaia* G-band observations using the V-band transformation provided by Evans et al. (2018). We also collected native V-band photometry from ASAS (Pojmanski 2002), ASAS-SN (Shappee et al. 2014; Jayasinghe et al. 2018), and Catalina (Torrealba et al. 2015; Drake et al. 2013a,b).

The normalizations and Doppler shift corrections were computed and applied using the National Optical As-

tronomy Observatory libraries for IRAF<sup>2</sup> (Image Reduction and Analysis Facility, Tody 1993). In-depth information regarding the radial velocity studies and phasing applied to this same sample can be found in Bono et al. (2020b).

It is important to note that automatic continuum normalisation methods must be employed with caution. Using high order functions to fit the continuum may result in the CaII K and H lines being made significantly shallower than they truly are. This can occur in spectrographs where the continuum emission in each echelle order is not very smooth and requires higher order fitting functions. For the du Pont sample, due to its large size, we developed an algorithm that used the smoothest echelle orders neighboring the order where the line of interest was present. These neighbor orders, devoid of any strong absorption features, were used to determine the best continuum fit, which was then applied to the order of interest.

All high resolution spectra that displayed measurable CaII K and at least one Balmer hydrogen line ( $H_\delta$ ,  $H_\gamma$ ,  $H_\beta$ ) were downgraded to  $R=2,000$  for the measurement of the equivalent widths necessary for the application of the  $\Delta S$  method (Sect. 4). Spectra of stars for which we have high resolution metallicity measurements from this work or For et al. (2011); Chadid et al. (2017); Sneden et al. (2017, hereafter cited together as For+Chadid+Sneden) form the calibrating sample. The rest were downgraded and rebinned to low resolution and included in the low resolution sample. Both samples are described in Sect. 3.

### 2.2. Low resolution spectroscopic dataset

We took advantage of the huge low resolution ( $R \approx 2,000$ ) spectroscopic dataset collected by the Sloan Extension for Galactic Exploration and Understanding Survey of the Sloan Digital Sky Survey (SEGUE-SDSS, Yanny et al. 2009), with the 2.5m Sloan Foundation Telescope at the Apache Point Observatory. The selection criteria for the spectroscopic sample were already discussed in detail in the first paper of this series Fabrizio et al. (2019, hereafter F19). Note that the F19 investigation was only based on fundamental RRLs so, in the present work, the RRc are added for the first time.

Most stars in the SEGUE-SDSS sample have only one or two exposures. To apply the new  $\Delta S$  calibration, we selected the spectra with SNR greater than 15, or that had SNR smaller than 15 but passed a visual inspection. The inspection was performed individually in order to

<sup>2</sup> The legacy code is now maintained by the community on GitHub at <https://iraf-community.github.io/>

**Table 1.** Identification, photometric characteristics, classification, and number of spectra for the CHR.

GaiaID (DR2)	Star	RA <sub>J2000</sub> (deg)	Dec <sub>J2000</sub> (deg)	Vmag (mag)	Vamp (mag)	P (day)	Class	Blazhko	N spectra
4224859720193721856	AA Aql	309.5628	-2.8903	11.86	1.16	0.36	RRab	?	1
2608819623000543744	AA Aqr	339.0161	-10.0153	12.93	0.99	0.61	RRab	?	1
1234729400256865664	AE Boo	221.8968	16.8453	10.62	0.45	0.31	RRc	?	5
3604450388616968576	AM Vir	200.8889	-16.6663	11.45	0.69	0.62	RRab	Yes	141
1191510003353849472	AN Ser	238.3794	12.9611	10.92	1.01	0.52	RRab	No	67

NOTE—Table 1 is published in its entirety in the machine-readable format. A portion is shown here for guidance regarding its form and content.

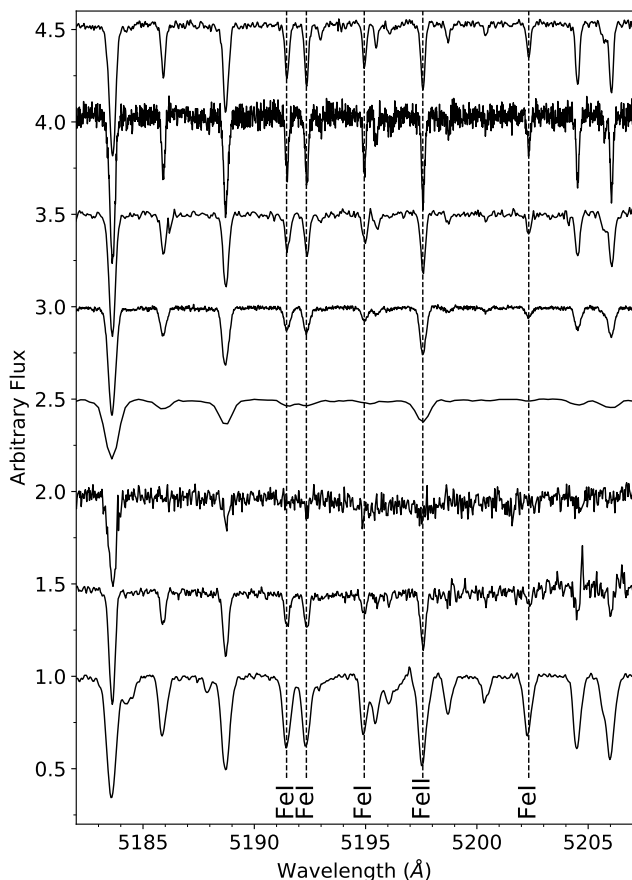


**Figure 1.** Examples of high resolution spectra from all spectrographs used in this work. From top to bottom: FEROS, HARPS, du Pont, UVES, X-shooter, Subaru HDS, STELLA, and SALT. The five first spectra are of V Ind ( $[\text{Fe}/\text{H}] = -1.63 \pm 0.03$ ) near phase 0.40. They are followed by random phase spectra for X Ari ( $[\text{Fe}/\text{H}] = -2.59 \pm 0.05$ ), DH Peg ( $[\text{Fe}/\text{H}] = -1.37 \pm 0.05$ ), and RW Tra ( $[\text{Fe}/\text{H}] = 0.13 \pm 0.06$ ). The dashed lines indicate the strongest iron lines present in this wavelength region.

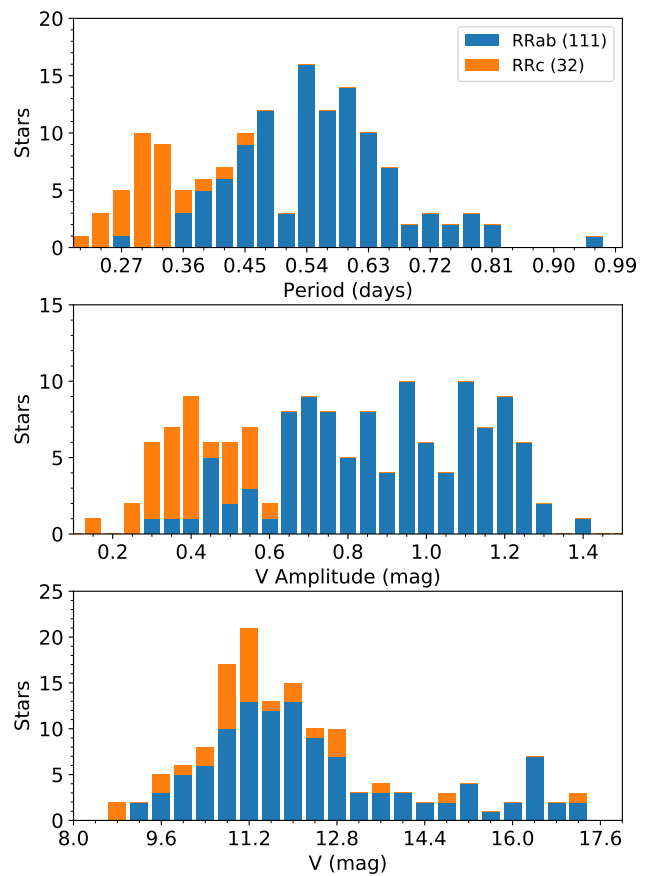


**Figure 2.** Period (top), visual amplitude (middle), and apparent visual magnitude (bottom) distributions for the RRab (blue) and RRc (orange) in the calibrating sample.

assess the quality of the CaII K and Balmer lines. We ended up with a sample of 6,299 spectra for 4,883 stars, of which 3,379 are RRab and 1,504 are RRc.

### 3. RR LYRAE SPECTROSCOPIC SAMPLES

The 143 stars (111 RRab, 32 RRc) for which we have HR metallicity measurements either from this work or from For+Chadid+Snedden, and also have  $\Delta S$  measurements in the new definition, were included in the calibrating sample (CHR). Those, together with 67 stars (59 RRab, 8 RRc) with HR measurements in the literature that could be brought onto our scale, were included in the high resolution (HR) sample. Finally, the low resolution (LR) sample contains 5,001 stars (3,439 RRab, 1,562 RRc) for which high resolution estimates were not available. Each sample is discussed in greater detail below.

### 3.1. High resolution calibrating sample

High resolution metallicities were derived from 171 measurements of 111 calibrating stars (91 RRab, 20 RRc, Tab. 3). Wherever possible, we analysed two exposures per star. In case there were no spectra with high enough SNR for abundance analysis (SNR  $\gtrsim 50$ ), we stacked spectra obtained at the same pulsation phase. The method for the determination of the pulsation periods for the whole sample is described in Bono et al. (2020b). Unlike the aforementioned work, however, we have defined the initial point of the pulsation cycle, i.e. phase zero, as the point where the magnitude along the decreasing branch of the light curve is equal to the mean magnitude of the variable (Braga et al. 2016). This initial point, also called the reference epoch, is arbitrary and only moves the light and velocity curves rigidly alongside the phase axis.

When stacking spectra, it is essential to make sure that all stacked spectra were collected at times where the stellar atmosphere had nearly the same thermodynamical configuration. Both observations (For et al. 2011) and theoretical models (Bono & Stellingwerf 1992) show that the atmosphere of RRL stars undergo temperature changes as large as 1,000 K. The clearest sign of different atmospheric temperatures between two spectra is a difference between the strength of the absorption lines, as well as their profiles. At lower temperatures, metallic lines are deeper and display larger EWs, while hydrogen lines are shallower and have smaller EWs.

With this in mind, when stacking spectra, we performed a phase selection as a first criterium. This ensures that the spectra were collected when the star was in the same moment of its pulsation cycle. Afterwards, we visually inspected all spectra to be stacked to verify they showed similar equivalent widths and profiles for the same lines. Verifying the equivalent widths guarantees that all combined spectra were collected roughly at the same pulsation phase. With this conservative approach, any precision concerns with the phasing do not

**Table 2.** List of FeI and FeII lines adopted in this work for the determination of atmospheric parameters.

Wavelength (Å)	Species	EP (eV)	log(gf) (dex)	Source
3763.78	26.0	0.989	-0.220	OBR91
3787.88	26.0	1.010	-0.840	OBR91
3815.84	26.0	1.484	0.240	OBR91
3820.42	26.0	0.858	0.160	OBR91
3825.88	26.0	0.914	-0.020	OBR91

NOTE—Table 2 is published in its entirety in the machine-readable format. A portion is shown here for guidance regarding its form and content. References: Bard et al. (1991, BAR91), Bard & Kock (1994, BAR94), Belmonte et al. (2017, BEL17), Blackwell et al. (1979, BLA79), Blackwell et al. (1982, BLA82), Blackwell et al. (1986, BLA86), Bridges & Kornblith (1974, BRI74), Den Hartog et al. (2014, DEN14), Kock et al. (1984, KOC84), Den Hartog et al. (2019, LAWLER), May et al. (1974, MAY74), Meléndez & Barbuy (2009, MELBAR), O’Brian et al. (1991, OBR91), Ruffoni et al. (2014, RUF14). The prefix *NIST* denotes the line had its transition parameters updated by NIST.

affect the quality of the stacking. Furthermore, any possible issues with the rest frame velocity correction are detected at this point in case the central wavelengths of absorption features fail to align. This visual inspection avoids the artificial line smearing caused by stacking spectra where the Doppler shift has not been properly accounted for.

We built a line list of 415 FeI and 56 FeII lines with the most up-to-date transition parameters found in the literature, with a preference for laboratory values. The parameters and references are presented in Tab. 2. The lines with a reference that begin with the prefix *NIST* had updated transition parameters taken from the National Institute of Standards and Technology (NIST) Atomic Spectra Database<sup>3</sup>. The list was carefully cleaned of blended lines using both the Moore et al. (1966) Solar spectrum atlas and synthetic spectra as a reference. The average number of useable lines in each spectrum was 66 for FeI and 19 for FeII (Fig. 3).

<sup>3</sup> Available at <https://www.nist.gov/pml/atomic-spectra-database>

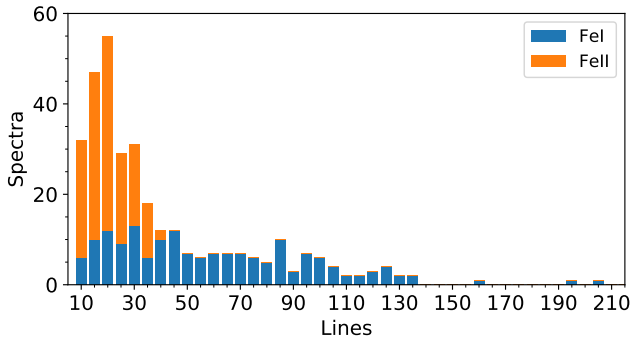


**Figure 3.** Distribution of the number of adopted FeI (blue) and FeII (orange) lines per spectrum. A total of 174 spectra of 111 stars (91 RRab, 20 RRc) were used.

Equivalent widths were measured manually using the IRAF task SPLIT to perform a Gaussian fit of the core of each line. There were no strong line asymmetries in any of the spectra used for this purpose. We performed an LTE line analysis using the 2019 release of MOOG<sup>4</sup> (Snedden 1973) paired with an interpolated grid of  $\alpha$ -enhanced ATLAS9 model atmospheres (Castelli & Kurucz 2003). Thus, we constrained the atmospheric parameters (effective temperature  $T_{\text{eff}}$ , surface gravity  $\log(g)$ , metallicity  $[\text{Fe}/\text{H}]$ , and microturbulent velocity  $\xi_t$ ) using the traditional approach, i.e. iteratively changing their values until achieving excitation equilibrium of FeI lines, ionization equilibrium of FeI and FeII lines, and no trend between the abundances of FeI lines and their reduced equivalent widths.

The final metallicity value for each star was taken as the simple mean of all its measurements. When more than one measurement was available for a given star, the uncertainty was taken to be the standard deviation of these measurements. This allowed us to compute a typical  $[\text{Fe}/\text{H}]$  uncertainty for each spectrograph by taking the median of these values for each instrument. This spectrograph-based median uncertainty was then adopted for the stars with a single spectrum, indicated by an asterisk on the last column of Tab. 5.

The median standard deviations for the uncertainties of the atmospheric parameters are  $\sigma(T_{\text{eff}}) = 150 \pm 136$  K,  $\sigma(\log(g)) = 0.43 \pm 0.16$  dex, and  $\sigma(\xi_t) = 0.14 \pm 0.25$  km s<sup>-1</sup>. To compute the impact of these values in the metallicity estimates, we have applied them to V Ind. We changed the temperature by 150 K, while keeping the other parameters in their final adopted value, and registered the difference  $\Delta[\text{Fe}/\text{H}]_{T_{\text{eff}}}$  for FeI and FeII lines this change created. We did the same for  $\log(g)$

and  $\xi_t$ , changing one parameter at a time and keeping the other parameters in their final value. Finally, we added in quadrature the three values of  $\Delta[\text{Fe}/\text{H}]$  for FeI and three for FeII. This resulted in a difference of 0.11 for FeI and 0.14 for FeII when compared to the final adopted atmosphere. Note that we show these values for reference only. The reason is that the sum in quadrature of correlated errors overestimates the final error, while it also does not take systematics into account. The metallicity errors derived by the standard deviation from multiple measurements of the same star are, therefore, a more robust uncertainty indicator and that is the value we have adopted, as described in the previous paragraph.

High resolution metallicities for an additional 32 stars (20 RRab, 12 RRc) were collected from three previous works using part of the Du Pont subsample (For+Chadid+Snedden). All their uncertainties are the standard deviation derived from multiple metallicity estimates in the same work. Stars with fewer than two measurements were not considered. The final adopted mean metallicities and their uncertainties are listed in Tab. 5. The estimates from the present work and of these three sources can be treated as a single homogeneous sample and produce a metallicity distribution ranging from -3.0 to 0.2 (Fig. 4). The entire metallicity range of RRL stars is, thus, covered in our calibrating sample of 143 RRL (111 RRab, 32 RRc).

In order to validate our high resolution measurements, we have compared them to all other such measurements for the same stars in the literature. This comparison is shown in Fig. 5 with the references listed in Tab. 4.

### 3.2. High resolution sample

In addition to the sample described above, we derived metallicities for a mixed mode pulsator from a total of ten X-shooter and two FEROS spectra individually, i.e. without stacking. It was not included in the CHR sample because we aimed to verify whether a mixed-mode pulsator would respond coherently to a  $\Delta S$  calibration made from a sample of both RRab and RRc.

A total of 134 field RRL have HR iron abundance estimates in the literature. Among these, 64 stars in eight studies are in common with our CHR sample, while two were in a study without any overlap with this work and were neglected. This allowed us to compute the shifts that need to be added to eight studies in order to bring their metallicity results into our scale (Fig. 5, Tab. 4). We have applied these shifts to another 67 stars that were in these studies, for which we have no metallicity estimate of our own. With the shifts applied, these 67 stars, alongside the CHR sample and the RRd

<sup>4</sup> The code and documentation can be found at <https://www.as.utexas.edu/~chris/moog.html>

**Table 3.** Atmospheric parameters derived in this work for each individual measurement.

GaiaID (DR2)	Star	Class	Spectrograph	$T_{\text{eff}}$ (K)	$\log(g)$ (dex)	$\xi_t$ ( $\text{km s}^{-1}$ )	[FeI/H] (dex)	$N_{\text{FeI}}$	[FeII/H] (dex)	$N_{\text{FeII}}$
4224859720193721856	AA Aql	RRab	SALT	$6610 \pm 65$	$2.70 \pm 0.01$	$2.52 \pm 0.04$	$-0.34 \pm 0.24$	206	$-0.34 \pm 0.22$	39
2608819623000543744	AA Aqr	RRab	UVES	$5840 \pm 80$	$1.52 \pm 0.06$	$3.51 \pm 0.13$	$-2.31 \pm 0.10$	37	$-2.31 \pm 0.12$	13
1234729400256865664	AE Boo	RRc	HARPS	$6630 \pm 75$	$2.04 \pm 0.04$	$2.79 \pm 0.05$	$-1.62 \pm 0.14$	64	$-1.62 \pm 0.10$	25
3604450388616968576	AM Vir	RRab	DuPont	$5870 \pm 50$	$1.52 \pm 0.06$	$3.32 \pm 0.06$	$-1.70 \pm 0.13$	87	$-1.70 \pm 0.17$	25
3626569264033312896	AS Vir	RRab	DuPont	$6030 \pm 75$	$1.66 \pm 0.10$	$3.44 \pm 0.11$	$-1.80 \pm 0.14$	38	$-1.80 \pm 0.22$	12

NOTE—Table 3 is published in its entirety in the machine-readable format. A portion is shown here for guidance regarding its form and content.

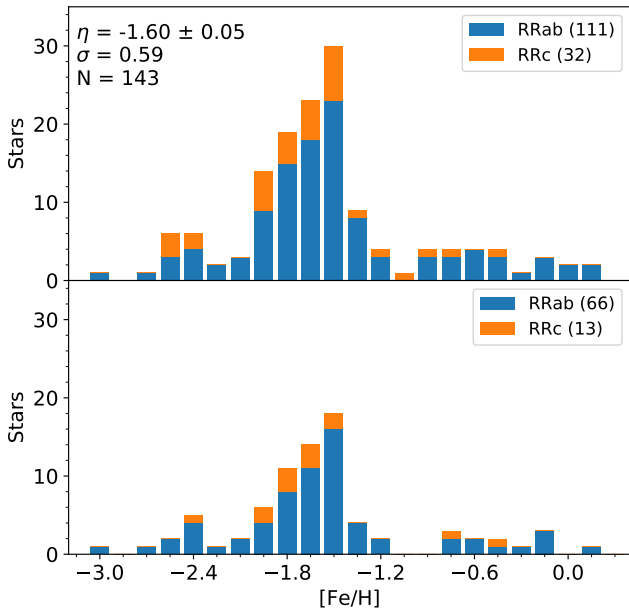


**Figure 4.** *Top:* Metallicity distribution of the 143 calibrating RRLs (RRab, blue; RRc, orange) based on high resolution spectra. These include new homogeneous measurements for 32 stars with previous measurements in the literature, and the results provided by For+Chadid+Snedden for another 32 stars. *Bottom:* Same as the top, but considering only the 79 stars for which we have provided high resolution metallicities for the first time.

mentioned above, form the HR sample with a total of 211 stars (170 RRab, 40 RRc, 1 RRd). It is the largest, most homogenous sample of high resolution metallicity measurements of field RRL stars. Indeed, it is almost a factor of two larger than any previous datasets of the same type in the literature (Magurno et al. 2018, 2019).

### 3.3. Low resolution sample

Together with the spectra used for the CHR sample we have had at our disposal another 298 high resolution spectra of 121 stars (62 RRab, 59 RRc). They were not

**Table 4.** Comparison between high resolution spectroscopic metallicities derived in this work and those derived in the literature. The number of stars in common is denoted by  $N$ , the median residuals by  $\Delta$ , and their standard deviation by  $\sigma$ . To bring metallicity values from these works into our scale, the shift  $\Delta$  must be added to them after they are put in the Asplund et al. (2009) Solar scale.

Source	$N$	$\Delta$	$\sigma$
A18	12	-0.06	0.20
C95	6	-0.14	0.12
F96	2	-0.06	0.09
G14	8	0.21	0.16
L13	12	-0.24	0.12
L96	9	-0.06	0.13
N13	5	-0.15	0.20
P15	10	-0.24	0.14
Total	64	-0.11	0.20

NOTE—References: Andrievsky et al. (2018, A18), Clementini et al. (1995, C95), Fernley & Barnes (1996, F96), Govea et al. (2014, G14), Liu et al. (2013, L13), Lambert et al. (1996, L96), Nemec et al. (2013, N13), Pancino et al. (2015, P15).

included among the calibrating RRLs because they had low SNR and were collected at different phases, making spectra stacking inviable. We degraded and rebinned their spectra to a spectral resolution  $R \approx 2,000$  and sampling  $\Delta \log(\lambda) = 0,0001$ , in order to mimic the native resolution of the SEGUE-SDSS spectra. This increased their SNR by a factor of four to five, approximately. Each star has its own individual  $[\text{Fe}/\text{H}]_{\Delta S}$  computed in the same way the values for the CHR sample were com-

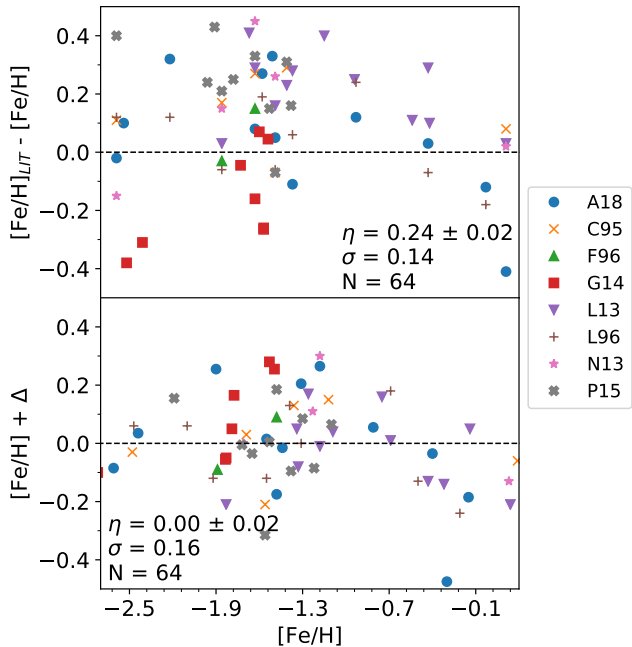


**Figure 5.** *Top:* Comparison of the high resolution spectroscopic metallicities adopted in this work with those available in the literature, transformed to the [Asplund et al. \(2009\)](#) Solar scale. *Bottom:* The same comparison once the shift  $\Delta$  is applied to the literature values, bringing them to our scale. The references and shifts are listed in Tab. 4.

**Table 5.** Adopted metallicities and uncertainties for each individual star in the CHR sample.

GaiaID (DR2)	Star	Class	[Fe/H] (dex)	Source
4224859720193721856	AA Aql	RRab	-0.42±0.11	1
2608819623000543744	AA Aqr	RRab	-2.31±0.04	1*
1234729400256865664	AE Boo	RRc	-1.62±0.09	1*
3604450388616968576	AM Vir	RRab	-1.77±0.09	1
1191510003353849472	AN Ser	RRab	0.05±0.01	4

NOTE—Table 5 is published in its entirety in the machine-readable format. A portion is shown here for guidance regarding its form and content. Metallicity and uncertainty sources: this work (1), [For et al. \(2011, 2\)](#), [Snedden et al. \(2017, 3\)](#), [Chadid et al. \(2017, 4\)](#). An asterisk denotes that the value was derived from a single measurement, and the uncertainty from the typical instrumental uncertainty. See text for details.

puted (Sect. 5). None of these stars has high resolution metallicity measurements in the literature.

The main reason why we developed a new  $\Delta S$  calibration is to apply it to low resolution spectra. Thus, we have joined these degraded spectra to the SEGUE-

SDSS low resolution spectra described in Sect. 2.2 for stars that were not added to the HR sample. This provided us with a total of 6,451 spectra for 5,001 stars (3,439 RRAb, 1,562 RRC) that form the low resolution (LR) sample.

#### 4. THE NEW $\Delta S$ DEFINITION

For the  $\Delta S$  measurements, all high resolution spectra for the stars in the CHR sample were degraded to  $R \approx 2,000$  and rebinned with  $\Delta \log(\lambda) = 0,0001$ . This ensures that they are similar to the native low resolution spectra for which the  $\Delta S$  method was developed. The equivalent widths of the lines of interest (Ca II K,  $H_\delta$ ,  $H_\gamma$ ,  $H_\beta$ ) were measured using an updated version of the code EWIMH ([Layden94](#), [Fabrizio et al. 2019](#)). We have adjusted the wavelength limits of the  $\Delta S$  definition in order to increase sensitivity to metallicity.

Absorption lines are formed across a small range of depths in the stellar atmosphere where the thermodynamical quantities allow the transition in question to occur. Strong lines may have significant wings that were formed at different layers and trace different environments. This is especially true in non-metallic, i.e. hydrogen, lines, often causing their very wide wings to swallow up metallic lines in their vicinity. The fraction of the equivalent width that comes from extended wings, therefore, does not necessarily represent the same thermodynamical quantities nor chemical abundance that the core of the line does.

The original [Layden94](#) definition considered the cores but not the wings of the hydrogen lines by using a measuring band with a width of 20 Å. For the Ca II K line, significantly weaker than the hydrogen lines, it employed a different measurement band depending on whether it was determined to be shallow or deep (see Fig. 3 of [Fabrizio et al. 2019](#)). For the former, the band had a width of 14 Å, and the latter of 20 Å. Both wide and narrow definitions included the full line with its wings and were careful to avoid nearby lines.

The Ca II line is flanked by two strong absorption features, namely the blend of the Ca II H at 3,968.5 Å with the  $H_\epsilon$  line at 3,970.0 Å, and the  $H_\zeta$  line at 3,889.1 Å. Both of them can have a dramatic effect on the continuum in very hot stars, with wings reaching as far as within  $\approx 15$  Å of the central wavelength of the Ca II K line. It is important to note that, as the hydrogen lines become deeper with increasing temperature, the metallic lines become shallower. Thus, it is reasonable to employ different measuring bands in each scenario. In very hot phases, however, the hydrogen lines may be so deep that the continuum near the Ca II K line is pulled down, so to say, by their wings. In such cases, even very nar-

row continuum bands will still be biased to lower values. For this reason, the original code used short continuum bands and employed a safeguard against the lowering of the continuum in hot stars: it allowed the bands to move in search of the maximum mean intensity, while keeping their length fixed. Departing from this definition, we tested combinations of the following scenarios:

- Using the original wavelength range for the hydrogen lines, which includes only their cores.
- Increasing the aforementioned range in order to include their wings.
- Considering multiple ranges for the Ca II K line, from the innermost 2 Å of the core, to the full line with its wings.
- Enabling and disabling the change between "wide" and "narrow" Ca II K lines.
- Changing the continuum band ranges in steps from -20% to +20%.
- Enabling and disabling the movement of the continuum band for the Ca II K line.

We found that including the wings of the H lines increases scatter without any significant effect on sensitivity to metallicity. This is partly due to the presence of metallic lines in the vicinity of the H lines, as noted by Layden94. On the other hand, increasing the range of the Ca II K line to always include both core and wings with the full 20 Å width for all measurements provided the best sensitivity without significant increase in scatter (Fig. 6) even for the "narrow" lines where continuum noise may creep into the measurements. This may be due to the fact that such noise in our data is much lower than in the data used by Layden94. As the change between "narrow" and "wide" Ca II K definitions did not cause significant improvement, we have disabled it.

Furthermore, we found that the continuum band range introduces only insignificant changes. The only exception is the continuum region around the Ca II K line due to the presence of the strong nearby absorption features. Therefore, we kept the original 15 Å range that gave enough points to define the continuum even in noisier spectra and saw no need to use different band widths on each side of the feature. We did not find a significant improvement when the continuum band was allowed to move, and so we kept its limits fixed. The final wavelength limits are shown in Fig. 7 and listed in Tab. 6. All measurements for the CHR sample are included in the supplementary Tab. 9.

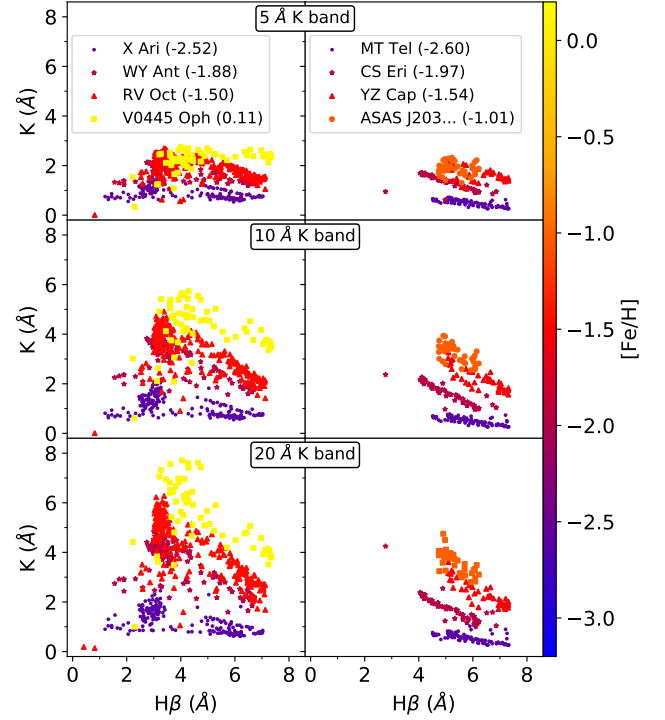


**Figure 6.** The HK plane for  $H\beta$  considering different widths (5, 10, and 20 Å) for the measurement band of the equivalent width of the CaII K line. A group of RRab (left) and RRC (right) stars are plotted with markers colored by metallicity according to the colorbar at the right edge of the figure. The considered stars are listed in the legend, with their respective high resolution metallicities between parentheses. The name for the RRC ASAS J203145-2158.7 is shortened for convenience.

**Table 6.** Wavelength intervals for the  $\Delta S$  measurements in the new calibration.

Line	Interval	Start	End
		(Å)	(Å)
CaIIK	Left continuum	3910.00	3925.00
	Equivalent width	3923.67	3943.67
	Right continuum	3940.00	3955.00
$H_\delta$	Left continuum	4010.00	4060.00
	Equivalent width	4091.74	4111.74
	Right continuum	4145.00	4195.00
$H_\gamma$	Left continuum	4230.00	4280.00
	Equivalent width	4330.47	4350.47
	Right continuum	4400.00	4450.00
$H_\beta$	Left continuum	4750.00	4800.00
	Equivalent width	4851.33	4871.33
	Right continuum	4920.00	4970.00

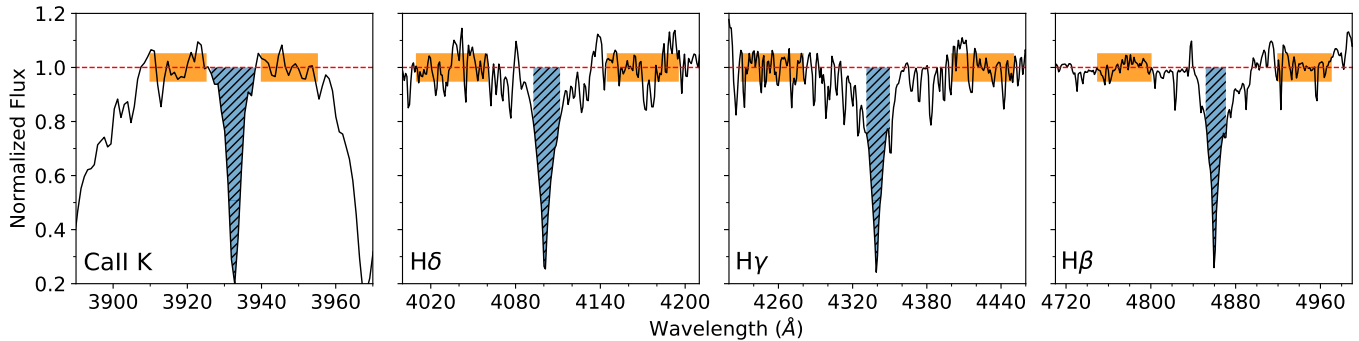


**Figure 7.** Wavelength ranges considered for the  $\Delta S$  measurements. In black, a du Pont spectrum for AN Ser ( $[\text{Fe}/\text{H}] = 0.05$ ) downgraded to a resolution  $R = 2,000$ . The red dashed line indicates the continuum level. The hatched blue area denotes the area considered in the equivalent width measurement for each line. The orange shaded area indicates the region considered for the continuum level definition. The precise wavelength intervals are displayed in Tab. 6.

#### 4.1. Changes in the EWIMH code

The EW measurements for the  $\Delta S$  method can and have been done with multiple codes, among which is the IDL code EWIMH. Alongside the wavelength limits discussed in the previous section, it is crucial to establish that, in our calibration, the EW is defined as the area between the observed spectrum and the continuum, derived numerically, and not the area under a Gaussian function fit to the data.

As mentioned above, we have disabled in the EWIMH code the change between "narrow" and "wide" definitions of the Ca II K line, and the freedom of movement of the continuum bands around it. These two features were part of the code itself, and should be disabled in order to comply with our new empirical calibration. The other changes we made to EWIMH were done in order to make the best use of all available spectra. These changes are not essential to the calibration, although we recommend them to be added to whatever code is employed in the EW measurements.

We adapted the computation of the continuum level and equivalent widths to be more robust against emission lines caused by cosmic rays or any instrumental defect that can mimic them such as dead pixels. Equivalent widths are defined as the width in wavelength of a rectangle with the height of the continuum that has the same area as the area between the absorption feature and the continuum level. Generally speaking, measurement codes consider the area of emission features as negative. This means that, when a cosmic ray produces a strong enough emission feature, there is a twofold issue: 1) the real area of the line is decreased by the presence of the emission; 2) if the emission defines an area above the continuum level, this area is subtracted from the equivalent width measurement.

We have introduced a change in the code so that it will discard points with a normalized flux greater than

one. This addresses the second issue by preventing negative area values and, in many cases, the first as well because most emissions do cross the continuum level. The missing value becomes instead a simple interpolation between its closest neighbors.

The continuum level is determined by using the mean flux inside the continuum bands at each side of the line of interest. We have inserted a condition that discards normalized fluxes greater than 1.25 in these bands, thus preventing emission features or defective pixels from biasing the continuum level determination.

## 5. THE NEW $\Delta S$ - $[\text{Fe}/\text{H}]$ CALIBRATION

A total of 6,327 spectra for 143 stars (111 RRab, 32 RRc) were included in the CHR sample. These are the stars for which we have homogeneous HR metallicity measurements (Sect. 3.1). They cover a wide range in period, pulsational amplitude (Fig. 2), and spectroscopic metallicity (Fig. 4).

We have verified that valid equivalent widths for individual lines in individual spectra remained in the range of 0.01 to 10.00 Å. Values outside these limits were most often from a distorted line or continuum, and so they were discarded. To compute the  $\Delta S$  index for each star, we took the median equivalent width of each feature of interest, considering all individual spectra for that star. Then, we performed a non-linear least squares fit using the IDL function CURVEFIT for a variety of analytical equations in the  $\Delta S$  index versus spectroscopic metallicity  $[\text{Fe}/\text{H}]$  plane. The process consists in applying the equation with free coefficients to the equivalent widths of interest, deriving one  $\Delta S$  value for each individual star. These values were then equated to their respective high resolution  $[\text{Fe}/\text{H}]$  measurements. The code attempts to minimize the residuals by repeating this process iteratively as it changes the coefficients.

This is a significant difference between our approach and that of Layden94. Indeed, Layden94 started from the K versus H plane, where K is the equivalent width of the Ca II K line, and H the average EW of the hydrogen lines of interest. While in the K versus H plane there are a series of roughly linear sequences with slopes that are metallicity-dependent, we have verified that the resulting  $\Delta S$  index from a polynomial fit done in this plane (i.e. the Layden94 equation, but with free coefficients) does not result in a tighter  $\Delta S$  versus  $[\text{Fe}/\text{H}]$  relation. This is discussed in more detail in Appendix A.

Other than the original Layden94 equation, with and without free coefficients, we have also attempted a variety of functions, such as variations of it using the logarithms, polynomials, sums of Gaussians, and Moffat functions. The minimum scatter was found with a polynomial with the form

$$[\text{Fe}/\text{H}]_{\Delta S} = c_0 + c_1 K + c_2 H_\delta + c_3 H_\gamma + c_4 H_\beta, \quad (1)$$

where K,  $H_\delta$ ,  $H_\gamma$ , and  $H_\beta$  are the equivalent widths in angstroms of the Ca II K and H lines as measured in the updated EWIMH code and using the newly defined wavelength ranges (Tab. 6). Here, the  $\Delta S$  index is already the metallicity estimate  $[\text{Fe}/\text{H}]_{\Delta S}$  and no further transformations are necessary.

The quality of the fit is similar for all combinations of H lines, therefore we provide the  $c_n$  coefficients for all seven cases in Tab. 7. Thus, if a given spectrum has only one or two hydrogen lines,  $[\text{Fe}/\text{H}]_{\Delta S}$  can still be estimated using the appropriate coefficients, with the missing H line having its corresponding  $c_n$  coefficient set to zero. The  $\Delta S$  versus spectroscopic metallicity plane for all combinations is shown in Fig. 8, while the corresponding values are listed in Tab. 8. Throughout this work, all comparisons performed against our own HR estimates or literature values were performed using the  $[\text{Fe}/\text{H}]_{\Delta S}$  equation for the full set of hydrogen lines.

The behavior of the Ca II K and hydrogen lines is peculiar in phases between 0.9 and 0.1, in particular in some RRab stars with larger pulsational amplitudes (e.g. Gillet & Fokin 2014; Gillet et al. 2016). In previous calibrations of the  $\Delta S$  method, these phases were neglected due to their association with the formation and propagation of shock waves, but this effect has never been investigated on a quantitative basis for the  $\Delta S$  method. We have verified that the removal of this phase interval from the CHR sample results in an improvement of only 0.02 in the scatter. This is also discussed in Sect. A. Removing the RRC had similarly negligible effects.

In order to properly classify the pulsation mode of an RRL star, multiple photometric observations and possibly a light curve template are needed so that a light curve with enough phase points can be built. Synchronizing observation time with pulsation phase requires both this detailed study and the availability of the telescope at the specific time window. If a star displays a mixed mode, or any other pulsational irregularity, this synchronization may not be possible at all. This is the reason we are providing a single calibration for both RRab and RRC at all phases. The negligible effect on the scatter when removing specific phases or separating the RRL by pulsation mode shows that previous studies of the RRLs of interest, in order to classify them and derive precise light curves, are unnecessary with this calibration.

Finally, the residuals do not show any clear trend with period or amplitudes, but are greater in the high metallicity regime. This is evident in the bottom panel of Fig. 9, which shows the difference between the HR  $[\text{Fe}/\text{H}]$  measurement and the low resolution  $[\text{Fe}/\text{H}]_{\Delta S}$  estimate, plotted against the HR  $[\text{Fe}/\text{H}]$ . The larger residuals for metal rich stars are also evident in Fig. 8, where a group of about five stars deviates from the main relation, displaying lower  $[\text{Fe}/\text{H}]_{\Delta S}$  values than expected. More data in the high metallicity regime are required to further constrain the nature of the spread in  $\Delta S$  values.

To constrain the accuracy of the new  $\Delta S$  calibration we estimated the metallicity distribution of the CHR sample and we found a median  $\eta = -1.53 \pm 0.00$  and a standard deviation of  $\sigma = 0.49$  (Fig. 9, top panel). This means that the  $\Delta S$  calibration can recover the metallicity distribution based on high resolution estimates for the same stars. Indeed, the latter has a median  $[\text{Fe}/\text{H}] = -1.60 \pm 0.00$  and  $\sigma = 0.59$  (Fig. 4). The median residual between both estimates is  $\eta = 0.05 \pm 0.03$ , with  $\sigma = 0.33$ .

## 6. VALIDATION

To verify the accuracy of the iron abundances based on the new  $\Delta S$  calibration we performed three independent tests using iron abundances based on literature values derived from both high and low resolution spectra.

### 6.1. Comparison with high resolution estimates in the literature

Concerning the iron abundances based on high resolution estimates, we performed two tests. First, we took advantage of the iron abundances for field RRLs based on HR spectra available in the literature. These have already been discussed during the validation of our high resolution metallicities (Sect. 4), and the shifts ( $\Delta$ )

**Table 7.** Coefficients for the new  $\Delta S$  equation (Eq. 1) for all combinations of hydrogen lines and the corresponding standard deviation of the residuals  $\sigma$ .

H lines	$c_0$	$c_1$	$c_2$	$c_3$	$c_4$	$\sigma$
H $\delta$ , H $\gamma$ , H $\beta$	$-3.84323 \pm 0.02438$	$0.36828 \pm 0.08481$	$-0.22182 \pm 0.11325$	$0.00433 \pm 0.08793$	$0.51481 \pm 0.18314$	0.33
H $\delta$ , H $\gamma$	$-3.75381 \pm 0.02682$	$0.39014 \pm 0.09433$	$-0.19997 \pm 0.10267$	$0.38916 \pm 0.20318$	–	0.37
H $\delta$ , H $\beta$	$-3.84160 \pm 0.02302$	$0.36798 \pm 0.05519$	$-0.21936 \pm 0.07134$	–	$0.51676 \pm 0.17720$	0.33
H $\gamma$ , H $\beta$	$-3.79074 \pm 0.02462$	$0.35889 \pm 0.07550$	–	$-0.21997 \pm 0.08967$	$0.50469 \pm 0.18582$	0.34
H $\delta$	$-3.48130 \pm 0.02690$	$0.36105 \pm 0.02689$	$0.14403 \pm 0.19890$	–	–	0.38
H $\gamma$	$-3.70799 \pm 0.02682$	$0.38127 \pm 0.02831$	–	$0.17973 \pm 0.20453$	–	0.38
H $\beta$	$-3.92067 \pm 0.02393$	$0.38194 \pm 0.03126$	–	–	$0.25898 \pm 0.18516$	0.35

**Table 8.** The  $[\text{Fe}/\text{H}]_{\Delta S}$  measurements for the CHR sample. Columns four to ten indicate between square brackets the combinations of hydrogen lines considered in the measurement.

GaiaID	Class	$N_{\text{spec}}$	[H $\delta$ , H $\gamma$ , H $\beta$ ]	[H $\delta$ , H $\gamma$ ]	[H $\delta$ , H $\beta$ ]	[H $\gamma$ , H $\beta$ ]	[H $\delta$ ]	[H $\gamma$ ]	[H $\beta$ ]
(DR2)			(dex)	(dex)	(dex)	(dex)	(dex)	(dex)	(dex)
15489408711727488	RRab	194	$-2.74 \pm 0.07$	$-2.43 \pm 0.05$	$-2.74 \pm 0.07$	$-2.73 \pm 0.07$	$-2.38 \pm 0.02$	$-2.43 \pm 0.02$	$-2.62 \pm 0.03$
77849374617106176	RRab	6	$-1.62 \pm 0.15$	$-1.56 \pm 0.14$	$-1.61 \pm 0.15$	$-1.56 \pm 0.15$	$-1.44 \pm 0.07$	$-1.51 \pm 0.08$	$-1.56 \pm 0.08$
80556926295542528	RRc	3	$-1.36 \pm 0.41$	$-1.49 \pm 0.58$	$-1.36 \pm 0.41$	$-1.27 \pm 0.45$	$-1.37 \pm 0.20$	$-1.40 \pm 0.28$	$-1.30 \pm 0.21$
630421935431871232	RRab	3	$-1.85 \pm 0.51$	$-1.93 \pm 0.48$	$-1.85 \pm 0.51$	$-1.80 \pm 0.47$	$-1.84 \pm 0.23$	$-1.88 \pm 0.23$	$-1.84 \pm 0.25$
1167409941124817664	RRc	1	$-1.68 \pm 0.00$	$-1.93 \pm 0.00$	$-1.68 \pm 0.00$	$-1.56 \pm 0.00$	$-1.77 \pm 0.00$	$-1.82 \pm 0.00$	$-1.67 \pm 0.00$

NOTE—Table 8 is published in its entirety in the machine-readable format. A portion is shown here for guidance regarding its form and content.

to move them in the current metallicity scale are listed in Tab. 4. They are included in the HR sample and contain 64 objects in common with the CHR sample. We found that the median difference between the new  $[\text{Fe}/\text{H}]_{\Delta S}$  and the literature high resolution estimates re-scaled into our scale is  $\eta = 0.12 \pm 0.04$ ,  $\sigma = 0.36$  (Fig. 10, top panel).

Second, we computed  $\Delta S$  metallicities for 12 RRLs that belong to Galactic globular clusters (GCs). The GC metallicities were provided by Carretta et al. (2009) in a new scale they constructed from high resolution estimates. No scale transformation was performed. The residuals of the comparison resulted in a median  $\eta = -0.08 \pm 0.04$  and  $\sigma = 0.16$  (Fig. 10, bottom panel).

### 6.2. Comparison with low resolution estimates in the literature

The RRab in the SEGUE-SDSS dataset were investigated in detail by F19 using the Layden94 definition. Considering the 2,385 RRab in common between both works, their estimates produce a metallicity distribution

with median  $[\text{Fe}/\text{H}]_{F19} = -1.60 \pm 0.01$  and  $\sigma = 0.40$ . Meanwhile, the new definition applied to the same stars provides  $[\text{Fe}/\text{H}]_{\Delta S} = -1.48 \pm 0.01$  and  $\sigma = 0.39$ . The top panel of Fig. 11 shows the residuals of this comparison.

Liu et al. (2020) constructed a large catalog of Galactic RRL with metallicities estimated from low resolution spectral matching. They made use of spectra from both SEGUE-SDSS and the LAMOST Experiment for Galactic Understanding and Exploration (Zhao et al. 2012). A total of 2,634 of their stars are included in our SEGUE-SDSS sample, allowing us to make a direct comparison between the two different approaches to metallicity estimation. Interestingly, their spectral matching technique relies on using precisely the Ca II K line, and the same three Balmer lines of the  $\Delta S$  method. The median difference between their values and the ones derived in this work is  $\eta = -0.23 \pm 0.00$  with  $\sigma = 0.24$  (Fig. 11, middle panel). The residuals are very similar for both the RRc ( $\eta = -0.21 \pm 0.01$ ,  $\sigma = 0.23$ ) and the RRab ( $\eta = -0.23 \pm 0.01$ ,  $\sigma = 0.24$ ). Note that the high resolution estimates they adopted to validate their method are, for 18

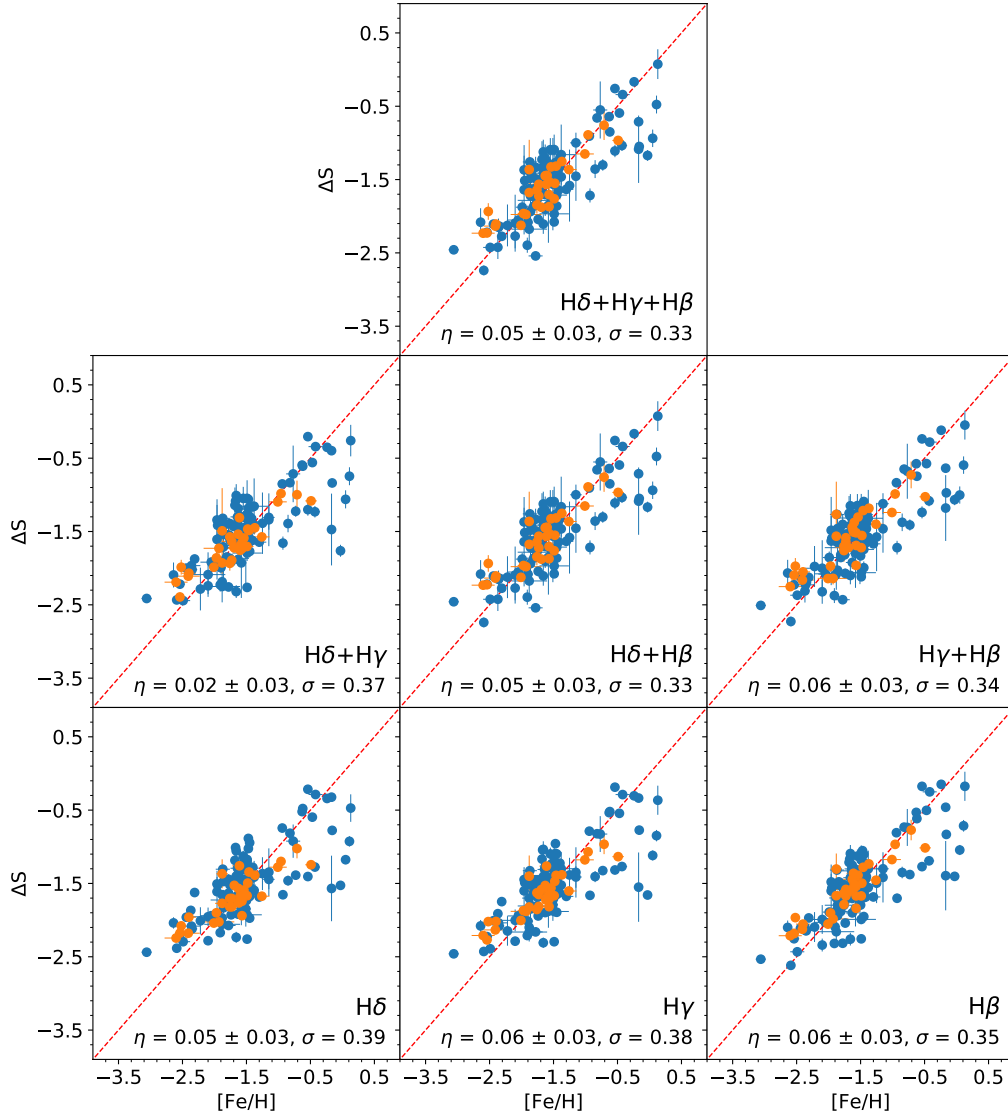


**Figure 8.** The  $\Delta S$  versus spectroscopic metallicity plane for all combinations of H lines, as indicated in the annotations inside each plot. The median residuals  $\eta$  and the standard deviation of residuals  $\sigma$  are also indicated for each case. RRab stars are plotted in blue and RRC in orange. The dashed red lines denote the identity line.

out of 19 stars, [Pancino et al. \(2015\)](#) and [Nemec et al. \(2013\)](#). These two works are included in our high resolution comparison and also present a similar shift (Fig. 5 and Tab. 4). Therefore, this scale difference of  $\approx -0.2$  between their results and ours is to be expected.

Finally, no validation would be complete without considering [Dambis \(2009\)](#) (D09), a compilation of RRL metallicities widely used in the literature. In order to keep the metallicity scale as homogeneous as possible, D09 adopted the values from Layden94 and [Layden et al. \(1996\)](#) wherever they were available, complementing them with other sources after these were transformed into the same Layden94 scale, which is the [Zinn & West \(1984\)](#) scale. In our comparison of 102 stars in common between their work and the new  $[\text{Fe}/\text{H}]_{\Delta S}$  estimates for

both the calibrating and LR samples, we found a shift of  $\eta=0.16\pm 0.03$ ,  $\sigma=0.30$ . However, to avoid having metallicities transformed into one scale, and then transformed once more into another scale, we will provide the corrections for the different D09 sources separately in a forthcoming paper.

### 6.3. Comparison with other low resolution spectrographs

We investigated the accuracy of the new  $[\text{Fe}/\text{H}]_{\Delta S}$  calibration in estimating the metallicity of individual RRLs when applied to native low resolution spectra collected with different instrument and telescope combinations. In particular, we have secured a set of LAMOST DR6 spectra for RRLs in common either with the LR sample

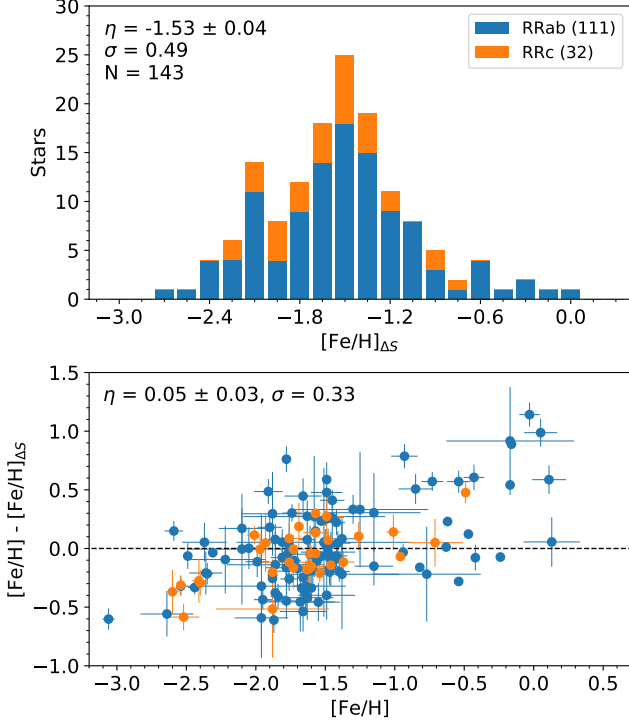


**Figure 9.** *Top:* The  $[\text{Fe}/\text{H}]_{\Delta S}$  distribution for the CHR sample. For reference, the distribution of high resolution measurements for the same sample is shown in the top panel of Fig. 4. *Bottom:* Residuals of the new  $\Delta S$  calibration versus spectroscopic metallicity. The RRab are plotted in blue, and the RRc in orange.

or with the HR sample. The new calibration was only applied to LAMOST spectra with SNR larger than ten in the region of the CaII K line. Afterwards, we visually inspected all the spectra with SNR between ten and twenty for a supplementary quality check before including them in the current analysis.

This resulted in a LAMOST sample of 569 low resolution spectra for 364 RRLs (203 RRab, 161 RRc). For 321 of these RRLs, we have  $[\text{Fe}/\text{H}]_{\Delta S}$  estimates coming from the LR sample, while for 43 of them we have  $[\text{Fe}/\text{H}]$  measurements in the HR sample. The  $[\text{Fe}/\text{H}]_{\Delta S}$  values derived from LAMOST spectra using the three hydrogen lines show no trend when compared to iron abundances based on the HR measurements (Fig. 12). The same outcome applies to the comparison with the LR sample, indeed, the residuals show a larger scatter ( $\sigma=0.28$  dex versus  $\sigma=0.19$  dex), but they are within the typical uncertainties of the method.

These good correlations indicate that the new  $[\text{Fe}/\text{H}]_{\Delta S}$  calibration when applied to low resolution spectra collected with different spectrographs provides metal abundances that are on the same scale. The same outcome applies to the comparison with the LR sam-

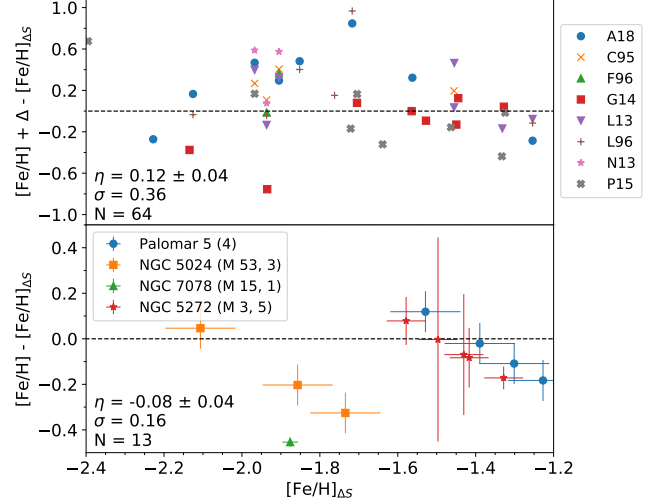


**Figure 10.** Comparison between the new  $[\text{Fe}/\text{H}]_{\Delta S}$  values and literature high resolution metallicities for RRL stars. *Top:* Field RRL with literature values brought to our scale by the addition of the corresponding shift ( $\Delta$ ). The references and shifts are listed in Tab. 4. *Bottom:* Globular cluster RRL considering the cluster metallicities derived by Carretta et al. (2009), which provides their value on a scale based on high resolution spectra. No shift has been applied to these values.

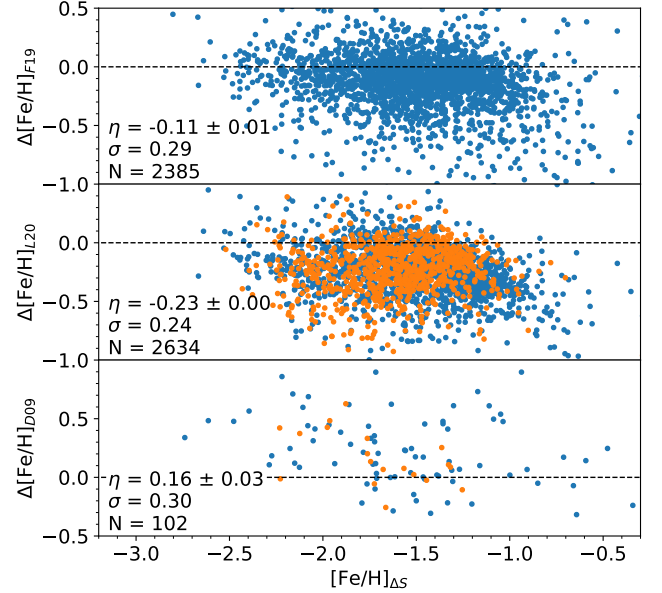


**Figure 11.** Difference  $\Delta[\text{Fe}/\text{H}] - [\text{Fe}/\text{H}]_{\Delta S}$  between the new  $[\text{Fe}/\text{H}]_{\Delta S}$  values and those derived by Fabrizio et al. (2019) with the SEGUE-SDSS dataset using the Layden94 definition ( $\Delta[\text{Fe}/\text{H}]_{F19}$ , top panel), Liu et al. (2020) with the SEGUE-SDSS and LAMOST datasets but using low resolution spectral matching ( $\Delta[\text{Fe}/\text{H}]_{L20}$ , middle panel), and the Dambis (2009) compilation ( $\Delta[\text{Fe}/\text{H}]_{D09}$ , bottom). The RRab are plotted in blue and the RRc in orange.

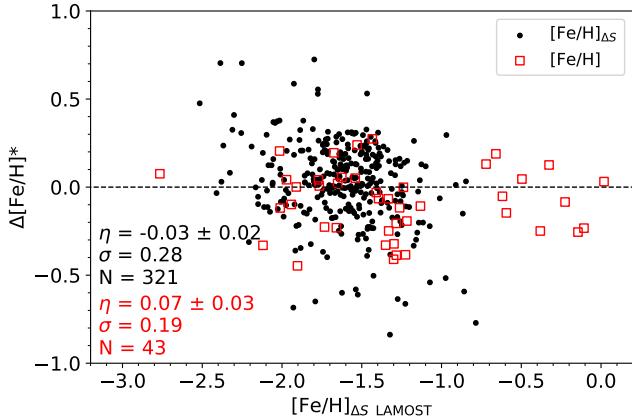


**Figure 12.** Residuals between  $[\text{Fe}/\text{H}]_{\Delta S}$  estimated with the new calibration applied to the RRLs of the LAMOST dataset, and the corresponding metallicities of the LR (black dots) and the HR (red squares) samples. The medians  $\eta$ , standard deviations  $\sigma$ , and sample sizes  $N$  are shown in black for the LR results, and in red for the HR results.

ple, indeed, the residuals show a larger scatter ( $\sigma=0.28$  dex versus  $\sigma=0.19$  dex), but they are within the typical uncertainties of the method.

In passing we also note that the SEGUE-SDSS and the LAMOST datasets when considered together, include eleven RRLs with a number of spectra randomly collected ranging from five to 15. To further investigate possible variations in metal abundances along the pulsation cycle, we applied the new calibration to these low resolution spectra collected with different spectrographs. We found a median standard deviation per RRL of  $\sim 0.15$  dex, in very good agreement with results based on the degraded high resolution spectra (see Tab. 8).

## 7. APPLICATION OF THE NEW $\Delta S$ CALIBRATION

### 7.1. Metallicity distribution of field RRL

Our new empirical  $[\text{Fe}/\text{H}]_{\Delta S}$  calibration allowed us, for the first time in the literature, to probe the metallicity distribution of the Galactic halo by applying the  $\Delta S$  method to both RRab and RRC stars. For this end, we employed the LR sample. It contains no stars in common with the HR sample, which we will analyse separately.

The resulting  $[\text{Fe}/\text{H}]_{\Delta S}$  distribution has a median  $\eta = -1.55 \pm 0.01$  and  $\sigma = 0.51$  (Fig. 13, top panel). The RRC display generally lower metallicities. Separating fundamental and first overtone pulsators results in medians that differ by 0.12, with the RRab peaking at  $[\text{Fe}/\text{H}]_{\Delta S} = -1.51 \pm 0.01$ , with  $\sigma = 0.50$ . Meanwhile, the values for the RRC are  $[\text{Fe}/\text{H}]_{\Delta S} = -1.63 \pm 0.01$  and  $\sigma = 0.50$ .

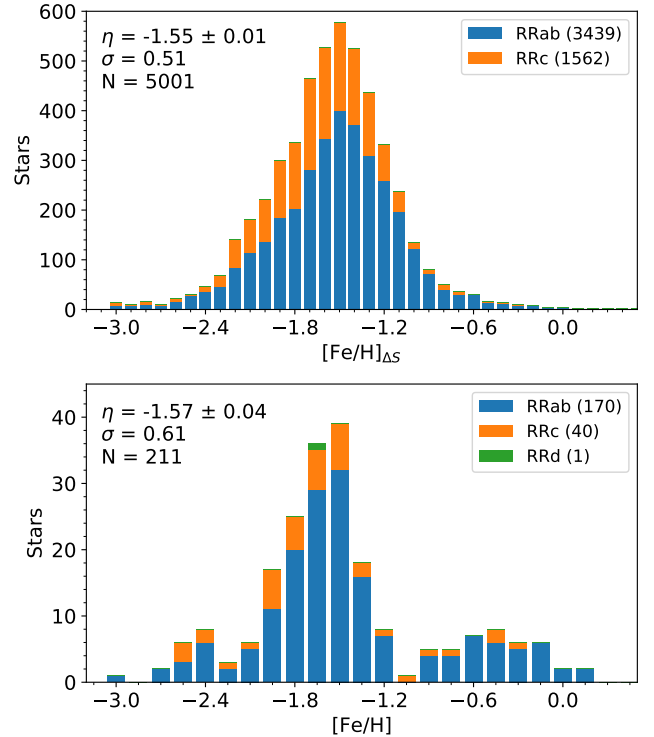


**Figure 13.** *Top:* Distribution of metallicities based on the new  $\Delta S$  definition for LR sample, consisting of 5,001 Galactic halo RRL stars (3,439 RRab, 1,562 RRC). *Bottom:* The HR sample, consisting of 211 RRL (170 RRab, 40 RRC, 1 RRd) from this work and the literature, with the latter brought into our scale. The RRab, RRC, and RRd are plotted, respectively, in blue, orange, and green.

The lower metallicity distribution for the RRC is also found in the results of Liu et al. (2020). Considering the stars in common between their work and ours, but their metallicity results, the RRab present  $\eta = -1.69 \pm 0.01$ ,  $\sigma = 0.35$ , while for the RRC the values are  $\eta = -1.80 \pm 0.01$ ,  $\sigma = 0.38$ . As mentioned in the previous section, there is a zero point shift of about 0.2 between their scale and ours that begins with the high resolution reference scale each work adopted.

Interestingly, the metallicity distribution as a whole is asymmetrical and cannot be adequately described by a single Gaussian, as is also the case for the kinematic distribution of the field halo stars (e.g. Lancaster et al. 2019). The slope in the metal-rich regime is steeper than in its metal-poor counterpart. In this context it is worth mentioning that the difference between the metallicity distribution of RRab and RRC is further supported by their asymmetry (skewness). Fig. 14 shows that the metal-rich tail of both RRab and RRC agrees quite well in the metal-rich regime. However, in the metal-poor regime the RRC display a broader peak and steeper slope ( $[\text{Fe}/\text{H}]_{\Delta S} \lesssim -1.8$ ). This evidence indicates that the pro-

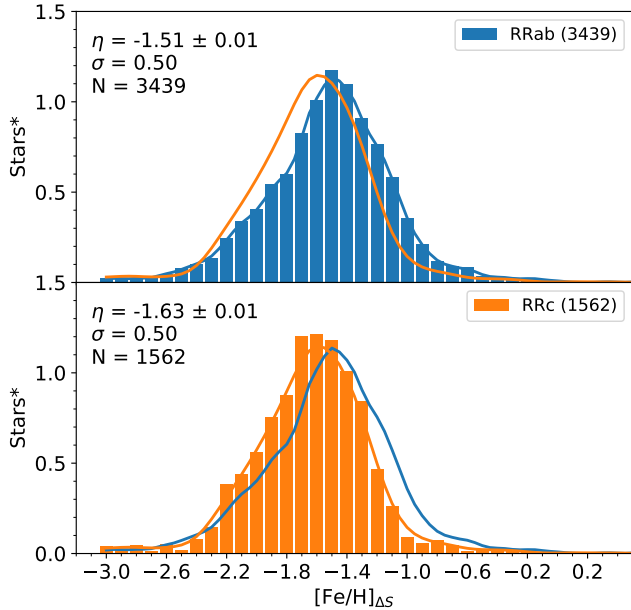


**Figure 14.** Area-normalized histograms of  $[\text{Fe}/\text{H}]_{\Delta S}$  for the LR sample. The RRAb are plotted in blue in the top panel, and the RRc in orange in the bottom panel. The full lines are the Gaussian-smoothed distributions for the RRAb and the RRc, in blue and orange, respectively. They are shown together on both panels for comparison.

duction rate of first overtone variables decreases as the metallicity of the stellar environment increases. This trend is expected because the metallicity is the most relevant parameter in shaping the morphology of the horizontal branch (Torelli et al. 2019), and in turn the sampling of the RRL instability strip (Bono et al. 1997, 2011).

### 7.2. The new $\Delta S$ calibration applied to a mixed mode variable

We also note that we have applied the new calibration to a field mixed mode variable (ASAS J183952-3200.9). On the basis of 10 high resolution spectra collected with X-Shooter and 2 with FEROS we estimated an iron abundance of  $[\text{Fe}/\text{H}] = -1.62 \pm 0.10$ . All 12 estimates were made from individual spectra, i.e. without stacking. The  $[\text{Fe}/\text{H}]_{\Delta S}$  abundance, based on the new  $\Delta S$  calibration applied to the same spectra but degraded to a spectral resolution of  $R=2,000$ , agrees quite well with  $[\text{Fe}/\text{H}]_{\Delta S} = -1.51 \pm 0.12$ . This is the first time that the metallicity of an RRd is estimated by using  $\Delta S$  and the remarkable agreement with the direct measurement further supports the plausibility of a single  $\Delta S$  calibration for all RRLs regardless of their pulsation mode.

## 8. SUMMARY AND FINAL REMARKS

We have provided a new calibration of the  $\Delta S$  method to derive low resolution spectroscopic metallicity estimates for RRL stars. It departs directly from the  $\Delta S$  versus  $[\text{Fe}/\text{H}]$  plane and makes use of homogeneous HR metallicity measurements for 143 RRLs (111 RRAb, 32 RRc) from a variety of spectrographs. The calibrating stars display a wide range of pulsational amplitudes and periods. They cover over three dex in iron abundance, including the metal-poor and metal-rich tails that were poorly sampled in previous works. The most metal-poor star in the CHR sample, with two high resolution measurements resulting in  $[\text{Fe}/\text{H}] = -3.06 \pm 0.08$ , may be among the most metal-poor RRLs ever identified (Wallerstein et al. 2009; Hansen et al. 2011). The metal-rich tail is similarly remarkable, with multiple stars presenting super-solar metallicities and pointing to a complex chemical enrichment history.

For the first time, this empirical calibration includes the full pulsation cycle as well as first overtone pulsators. Therefore, it is not necessary to classify the pulsation mode of the RRL of interest, nor execute timed observations in order to gather the data at specific phase intervals. This means no detailed knowledge of the light curve is required.

While we suggest preference be given to the calibration with all Balmer lines ( $H_\delta$ ,  $H_\gamma$ ,  $H_\beta$ ) when possible, followed by combinations that include  $H_\beta$ , we also provide coefficients for all combinations of one or two of these lines. We have employed both SEGUE-SDSS ( $R \approx 2,000$ ) and LAMOST ( $R \approx 1,500$ ) spectra to investigate whether the new calibration is valid for low resolution spectra collected with different spectrographs. Our findings support that the new calibration can be applied to different spectrographs and resolutions. This means that there is no need for transformations between different equivalent widths systems in order to obtain metallicity estimates within the typical uncertainties of the method. We also provide 211 reference stars covering a wide range in metallicity in high resolution, 144 of which have also  $[\text{Fe}/\text{H}]_{\Delta S}$  estimates based on all combinations of Balmer lines. This is the largest sample of high resolution measurements for field RRL stars in the literature and can be used to anchor any future works in our metallicity scale.

We have applied the new  $\Delta S$  calibration to a sample of 5,001 field RRLs (3,439 RRAb, 1,562 RRc) with either SEGUE-SDSS low resolution spectra or high resolution spectra downgraded and rebinned in order to mimic the SEGUE-SDSS spectra. This resulted in a distribution with median  $\eta = -1.55 \pm 0.01$  and  $\sigma = 0.51$ , in good agreement with previous studies of halo RRLs. For comparison, the HR sample described above has a dis-

tribution with  $\eta=-1.57\pm 0.04$  and  $\sigma=0.61$ . In both cases, the distribution for the RRc alone peaks at slightly lower metallicities than the RRab. Furthermore, the metallicity distributions of the RRab and RRc, when considered separately, have different profiles in the metal-poor regime. Indeed, the slope of the distribution is shallower for the RRc. This difference in the profiles and the  $\approx 0.1$  difference in the peaks of the two distributions support the theoretical scenario of a steady decrease in the production of RRc as the metallicity of the stellar environment increases.

#### ACKNOWLEDGMENTS

It is a real pleasure to thank the anonymous referee for her/his positive remarks concerning the content and the results of this investigation and for her/his pertinent suggestions that improved the readability of the paper.

This research has made use of the National Aeronautics and Space Administration (NASA) Astrophysics Data System, the National Institute of Standards and Technology (NIST) Atomic Spectra Database, the JVO Portal<sup>5</sup> operated by ADC/NAOJ, and the ESO Science Archive Facility.

Based on observations made with the Italian Telescopio Nazionale Galileo (TNG) operated on the island of La Palma by the Fundación Galileo Galilei of the INAF (Istituto Nazionale di Astrofisica) at the Spanish Observatorio del Roque de los Muchachos of the Instituto de Astrofísica de Canarias.

Some of the observations reported in this paper were obtained with the Southern African Large Telescope (SALT).

Based on observations collected at the European Organisation for Astronomical Research in the Southern Hemisphere under ESO programmes 0100.D-0339, 0101.D-0697, 0102.D-0281, 076.B-0055, 077.B-0359, 077.D-0633, 079.A-9015, 079.D-0262, 079.D-0462, 079.D-0567, 082.C-0617, 083.B-0281, 083.C-0244, 094.B-0409, 095.B-0744, 097.A-9032, 098.D-0230, 189.B-0925, 267.C-5719, 297.D-5047, 67.D-0321, 67.D-0554, 69.C-0423, 71.C-0097, 0100.D-0273, 083.C-0244, 098.D-0230.

Guoshoujing Telescope (the Large Sky Area Multi-Object Fiber Spectroscopic Telescope LAMOST) is a National Major Scientific Project built by the Chinese Academy of Sciences. Funding for the project has been provided by the National Development and Reform Commission. LAMOST is operated and managed by the National Astronomical Observatories, Chinese Academy of Sciences.

Funding for the SDSS and SDSS-II has been provided by the Alfred P. Sloan Foundation, the Participating Institutions, the National Science Foundation, the U.S. Department of Energy, the National Aeronautics and Space Administration, the Japanese Monbukagakusho, the Max Planck Society, and the Higher Education Funding Council for England. The SDSS Web Site is <http://www.sdss.org/>. The SDSS is managed by the Astrophysical Research Consortium for the Participating Institutions. The Participating Institutions are the American Museum of Natural History, Astrophysical Institute Potsdam, University of Basel, University of Cambridge, Case Western Reserve University, University of Chicago, Drexel University, Fermilab, the Institute for Advanced Study, the Japan Participation Group, Johns Hopkins University, the Joint Institute for Nuclear Astrophysics, the Kavli Institute for Particle Astrophysics and Cosmology, the Korean Scientist Group, the Chinese Academy of Sciences (LAMOST), Los Alamos National Laboratory, the Max-Planck-Institute for Astronomy (MPIA), the Max-Planck-Institute for Astrophysics (MPA), New Mexico State University, Ohio State University, University of Pittsburgh, University of Portsmouth, Princeton University, the United States Naval Observatory, and the University of Washington.

We acknowledge financial support from US NSF under Grants AST-1714534 (MM, JPM) and AST1616040 (CS). EKG, BL, and ZD were supported by the Deutsche Forschungsgemeinschaft (DFG, German Research Foundation) - Project-ID 138713538 - SFB 881 ("The Milky Way System", subprojects A03, A05, A11). EV acknowledges the Excellence Cluster ORIGINS Funded by the Deutsche Forschungsgemeinschaft (DFG, German Research Foundation) under Germany's Excellence Strategy - EXC - 2094 - 390783311.

#### APPENDIX

<sup>5</sup> <http://jvo.nao.ac.jp/portal/>

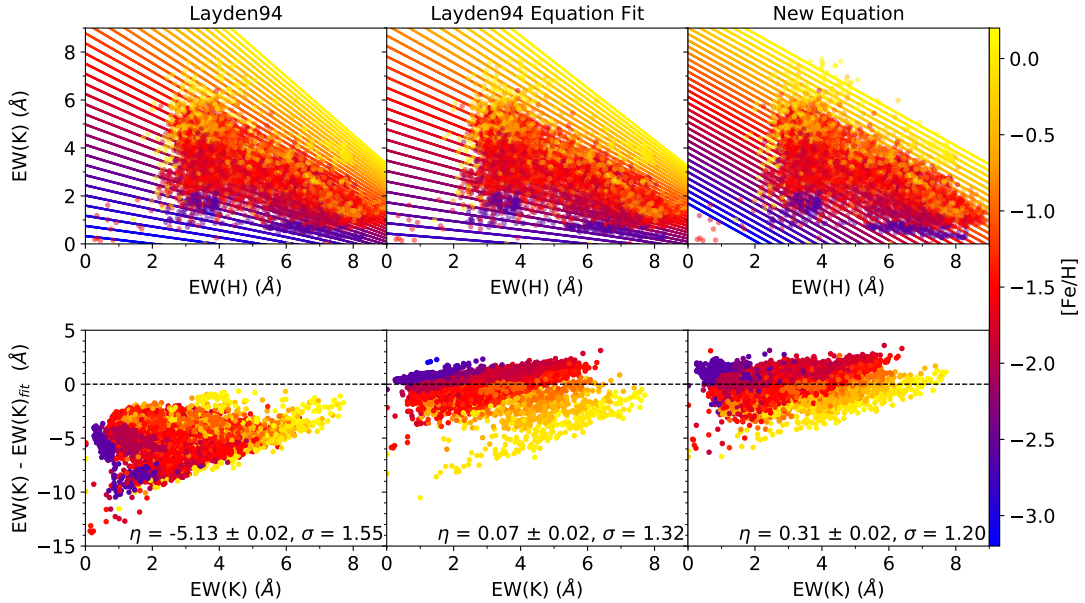


**Figure 15.** The HK plane (top) and residuals of the  $\Delta S$  (bottom) for the CHR sample considering three cases: the original Layden94 equation (left), a fit of the Layden94 equation with new coefficients (middle), and the new equation (right). The points are the measured EW values in the new definition of wavelength ranges. The lines in the top panels are the predicted Ca II K equivalent width considering each equation for a range of metallicity values. Data points and analytical lines are colored by high resolution metallicity according to the colorbar at the right edge of the figure.

#### A. EQUIVALENT WIDTH DEPENDENCE ON METALLICITY AND PHASE

This work departed directly from the  $\Delta S$  versus spectroscopic metallicity plane in order to find the best analytical equation and parameters relating these two quantities. The original Layden94 equation, however, departed from a polynomial fit in the HK plane, resulting in a relation with the form

$$K = a + bH + c[Fe/H] + dH[Fe/H], \quad (\text{A1})$$

where  $a$  to  $d$  are constants,  $K$  the EW of the Ca II K line and  $H$  the mean EW for the three H lines. This is a very reasonable strategy as there is a clear pattern for the RRL in this plane, with stars of similar metallicity clustering in a somewhat linear fashion, with a slope and intercept that increases with metallicity. Thus, we attempted a new fit of the coefficients of this equation. The result created a larger overall scatter in the  $\Delta S$ -[Fe/H] plane with  $\sigma_r$  greater by 0.12. Furthermore, it could not trace the metal rich regime. The polynomial equation derived in this work, on the other hand, does not contain a metallicity-dependent slope in the HK plane. This in turn yielded a tighter relation that can reach the metal rich regime (Fig. 6). A comparison in the  $\Delta S$ -[Fe/H] plane between the polynomial fit adopted in this work and the Layden94 equation with new coefficients is shown in Fig. 18.

The original Layden94 definition did not include rising branch phases due to the shock waves that occur at this point of the pulsation cycle and can distort the profile of the Balmer lines. This phase avoidance introduces the burdensome necessity of properly phasing the RRL and timing observations in such a way as to avoid these phases. Adequate light curves and reference epochs require multiple previous observations that may not be readily available. Furthermore, as discussed previously, the duration of the line-distorting shock waves is very brief.

In the HK plane, stars in these phases occupy a region underneath the area created by the other phases, effectively creating a "loop" that invades a lower metallicity region. Fig. 16 illustrates the origin of the "loops". Their lower sequence is caused by not only a sharp peak in the EW of the H lines, but also a sudden dip in the EW of the Ca II K line. Both the H and the Ca II K lines are strongly responsive to the effective temperature, albeit in opposite directions, i.e. the EW of H lines increases with temperature, while that of the Ca II K decreases. Deriving metallicities from a combination of these lines, therefore, relies on this mirrored effect that nullifies the influence of the temperature on the equivalent width of the Ca II K, effectively isolating the metallicity impact. However, the peak of the H lines and the dip of the Ca II K lines in EW are not perfectly synchronized, with the latter occurring slightly earlier. Thus, at

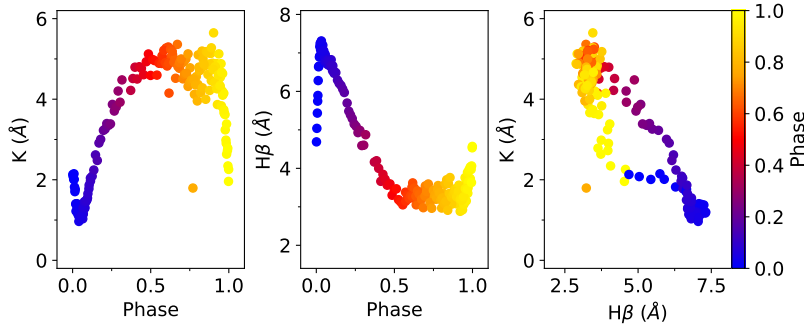


**Figure 16.** Equivalent widths for the Ca II K (left) and  $H\beta$  (middle) lines, and the HK plane (right) for HH Pup. Symbols are colored according to phase.

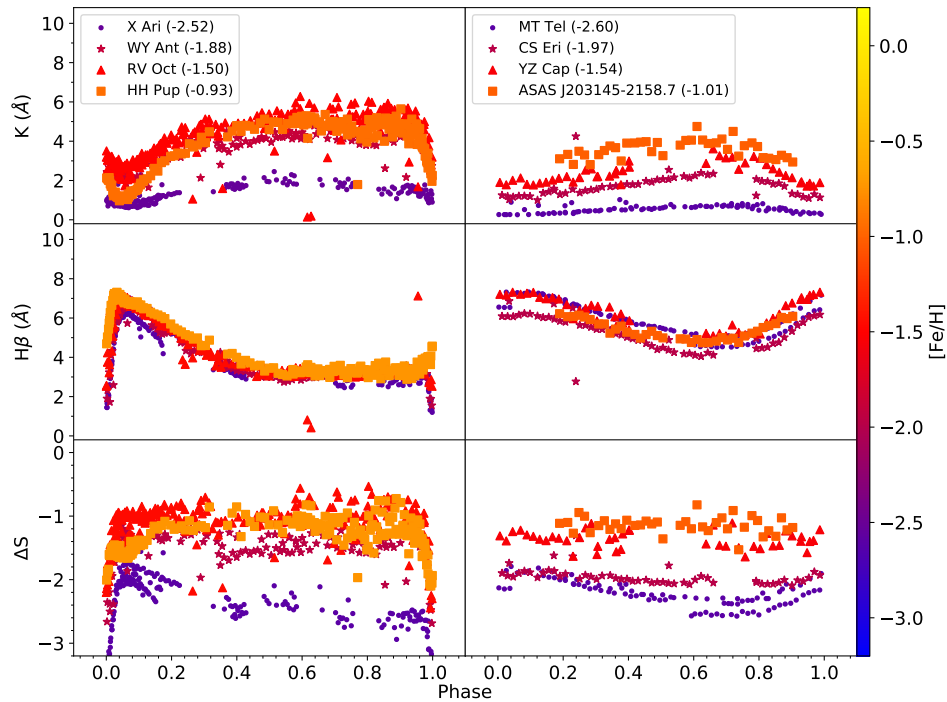


**Figure 17.** Behavior of the equivalent width of the Ca II K line (top),  $H\beta$  line (middle), and  $\Delta S$  value (bottom) across the entire pulsation cycle for three RRAb (left panels) and three RRC (right panels). The points are colored by metallicity according to the colorbar on the right edge of the figure. The considered stars are listed in the legend, with their respective high resolution metallicities between parentheses.

phase 0.9 to 0.1, we observe a sudden drop of any value that relates these two quantities, as evident in the bottom panels of Fig. 17.

Note that the EW variation of the lines of interest in the RRC is significantly smoother. This is also true for their light curves, which are almost sinusoidal while those of their fundamental mode counterparts are sawtooth-shaped. The Ca II K line dip is not identical among RRAb stars either. There is some evidence that more metal rich stars will display a deeper dip, but other characteristics such as pulsational amplitude may play a role.

In order to investigate the effect of phases between 0.9 and 0.1 in the final  $\Delta S$  value, we have removed them from the sample and performed a new fit of the coefficients of the polynomial equation and of the Layden94 equation. We found that this produced slightly smaller median residuals and slightly larger scatter for the new equation (Fig. 18). For the Layden94 equation, the phase cut caused both quantities to increase over 0.2. This phase interval, therefore, only has minimal effect on the  $\Delta S$  computation with the new equation.

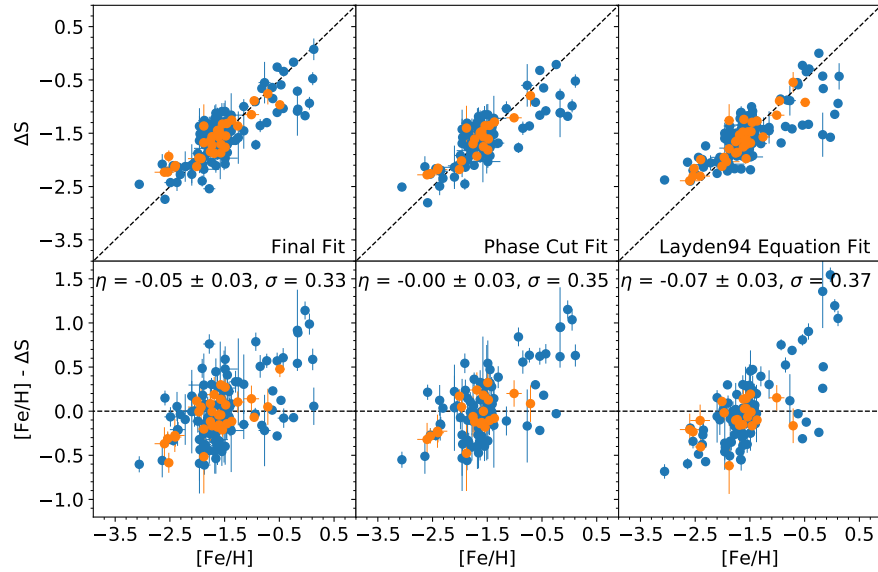


**Figure 18.** The  $\Delta S$ -[Fe/H] plane (top) and residuals (bottom) for three cases considering all H lines: the final polynomial fit adopted in this work (left), the polynomial fit derived from the sample with phases between 0.1 and 0.9 (middle), and the fit of the Layden94 equation with new coefficients (right). The RRab are plotted in blue and the RRC in orange.

**Table 9.** Individual measurements of the equivalent widths of interest for the CHR sample.

GaiaID (DR2)	MJD (day)	CaII K (Å)	H $\delta$ (Å)	H $\gamma$ (Å)	H $\beta$ (Å)
15489408711727488	2455454.81452	2.14±0.57	4.05±0.62	4.26±0.38	3.24±0.35
15489408711727488	2455454.82015	1.95±0.73	3.97±0.46	4.34±0.52	3.22±0.33
15489408711727488	2455454.82434	1.94±0.55	4.26±0.46	4.08±0.48	3.26±0.54
15489408711727488	2455454.85236	1.89±0.85	3.86±0.48	4.18±0.70	3.09±0.40
15489408711727488	2455454.85655	2.09±0.72	3.67±0.55	3.87±0.58	2.96±0.41

NOTE—Table 9 is published in its entirety in the machine-readable format. A portion is shown here for guidance regarding its form and content.

## B. SUPPLEMENTARY TABLES

### REFERENCES

- Andrievsky, S., Wallerstein, G., Korotin, S., et al. 2018, *PASP*, 130, 024201, doi: [10.1088/1538-3873/aa9783](https://doi.org/10.1088/1538-3873/aa9783)
- Asplund, M., Grevesse, N., Sauval, A. J., & Scott, P. 2009, *ARA&A*, 47, 481, doi: [10.1146/annurev.astro.46.060407.145222](https://doi.org/10.1146/annurev.astro.46.060407.145222)
- Bard, A., Kock, A., & Kock, M. 1991, *A&A*, 248, 315
- Bard, A., & Kock, M. 1994, *A&A*, 282, 1014
- Belmonte, M. T., Pickering, J. C., Ruffoni, M. P., et al. 2017, *ApJ*, 848, 125, doi: [10.3847/1538-4357/aa8cd3](https://doi.org/10.3847/1538-4357/aa8cd3)
- Blackwell, D. E., Booth, A. J., Haddock, D. J., Petford, A. D., & Leggett, S. K. 1986, *MNRAS*, 220, 549, doi: [10.1093/mnras/220.3.549](https://doi.org/10.1093/mnras/220.3.549)
- Blackwell, D. E., Petford, A. D., & Shallis, M. J. 1979, *MNRAS*, 186, 657, doi: [10.1093/mnras/186.4.657](https://doi.org/10.1093/mnras/186.4.657)
- Blackwell, D. E., Petford, A. D., Shallis, M. J., & Simmons, G. J. 1982, *MNRAS*, 199, 43, doi: [10.1093/mnras/199.1.43](https://doi.org/10.1093/mnras/199.1.43)

- Bono, G., Caputo, F., Castellani, V., & Marconi, M. 1997, *A&AS*, 121, 327, doi: [10.1051/aas:1997289](https://doi.org/10.1051/aas:1997289)
- Bono, G., Caputo, F., Castellani, V., et al. 2003, *MNRAS*, 344, 1097, doi: [10.1046/j.1365-8711.2003.06878.x](https://doi.org/10.1046/j.1365-8711.2003.06878.x)
- Bono, G., Dall’Ora, M., Caputo, F., et al. 2011, in *RR Lyrae Stars, Metal-Poor Stars, and the Galaxy*, ed. A. McWilliam, Vol. 5, 1. <https://arxiv.org/abs/1108.5372>
- Bono, G., & Stellingwerf, R. F. 1992, *Mem. Soc. Astron. Italiana*, 63, 357
- Bono, G., Iannicola, G., Braga, V. F., et al. 2019, *ApJ*, 870, 115, doi: [10.3847/1538-4357/aaf23f](https://doi.org/10.3847/1538-4357/aaf23f)
- Bono, G., Braga, V. F., Fiorentino, G., et al. 2020a, arXiv e-prints, arXiv:2009.06985. <https://arxiv.org/abs/2009.06985>
- Bono, G., Braga, V. F., Crestani, J., et al. 2020b, *ApJL*, 896, L15, doi: [10.3847/2041-8213/ab9538](https://doi.org/10.3847/2041-8213/ab9538)
- Braga, V. F., Stetson, P. B., Bono, G., et al. 2016, *AJ*, 152, 170, doi: [10.3847/0004-6256/152/6/170](https://doi.org/10.3847/0004-6256/152/6/170)
- . 2018, *AJ*, 155, 137, doi: [10.3847/1538-3881/aaadab](https://doi.org/10.3847/1538-3881/aaadab)
- Bridges, J. M., & Kornblith, R. L. 1974, *ApJ*, 192, 793, doi: [10.1086/153118](https://doi.org/10.1086/153118)
- Butler, D. 1975, *ApJ*, 200, 68, doi: [10.1086/153761](https://doi.org/10.1086/153761)
- Butler, D., Carbon, D., & Kraft, R. P. 1976, *ApJ*, 210, 120, doi: [10.1086/154809](https://doi.org/10.1086/154809)
- Butler, D., Kinman, T. D., & Kraft, R. P. 1979, *AJ*, 84, 993, doi: [10.1086/112503](https://doi.org/10.1086/112503)
- Carretta, E., Bragaglia, A., Gratton, R., D’Orazi, V., & Lucatello, S. 2009, *A&A*, 508, 695, doi: [10.1051/0004-6361/200913003](https://doi.org/10.1051/0004-6361/200913003)
- Castelli, F., & Kurucz, R. L. 2003, in *IAU Symposium*, Vol. 210, *Modelling of Stellar Atmospheres*, ed. N. Piskunov, W. W. Weiss, & D. F. Gray, A20. <https://arxiv.org/abs/astro-ph/0405087>
- Chadid, M., Sneden, C., & Preston, G. W. 2017, *ApJ*, 835, 187, doi: [10.3847/1538-4357/835/2/187](https://doi.org/10.3847/1538-4357/835/2/187)
- Chadid, M., Vernin, J., & Gillet, D. 2008, *A&A*, 491, 537, doi: [10.1051/0004-6361:200810270](https://doi.org/10.1051/0004-6361:200810270)
- Clementini, G., Carretta, E., Gratton, R., et al. 1995, *AJ*, 110, 2319, doi: [10.1086/117692](https://doi.org/10.1086/117692)
- Crause, L. A., Sharples, R. M., Bramall, D. G., et al. 2014, in *Society of Photo-Optical Instrumentation Engineers (SPIE) Conference Series*, Vol. 9147, *Ground-based and Airborne Instrumentation for Astronomy V*, 91476T, doi: [10.1117/12.2055635](https://doi.org/10.1117/12.2055635)
- Cropper, M., Katz, D., Sartoretti, P., et al. 2018, *A&A*, 616, A5, doi: [10.1051/0004-6361/201832763](https://doi.org/10.1051/0004-6361/201832763)
- Dambis, A. K. 2009, *MNRAS*, 396, 553, doi: [10.1111/j.1365-2966.2009.14733.x](https://doi.org/10.1111/j.1365-2966.2009.14733.x)
- Dambis, A. K., Berdnikov, L. N., Kniazev, A. Y., et al. 2013, *MNRAS*, 435, 3206, doi: [10.1093/mnras/stt1514](https://doi.org/10.1093/mnras/stt1514)
- Den Hartog, E. A., Lawler, J. E., Sneden, C., Cowan, J. J., & Brukhovesky, A. 2019, *ApJS*, 243, 33, doi: [10.3847/1538-4365/ab322e](https://doi.org/10.3847/1538-4365/ab322e)
- Den Hartog, E. A., Ruffoni, M. P., Lawler, J. E., et al. 2014, *ApJS*, 215, 23, doi: [10.1088/0067-0049/215/2/23](https://doi.org/10.1088/0067-0049/215/2/23)
- Drake, A. J., Catelan, M., Djorgovski, S. G., et al. 2013a, *ApJ*, 763, 32, doi: [10.1088/0004-637X/763/1/32](https://doi.org/10.1088/0004-637X/763/1/32)
- . 2013b, *ApJ*, 765, 154, doi: [10.1088/0004-637X/765/2/154](https://doi.org/10.1088/0004-637X/765/2/154)
- Drake, A. J., Djorgovski, S. G., Catelan, M., et al. 2017, *MNRAS*, 469, 3688, doi: [10.1093/mnras/stx1085](https://doi.org/10.1093/mnras/stx1085)
- Evans, D. W., Riello, M., De Angeli, F., et al. 2018, *A&A*, 616, A4, doi: [10.1051/0004-6361/201832756](https://doi.org/10.1051/0004-6361/201832756)
- Fabrizio, M., Bono, G., Braga, V. F., et al. 2019, *ApJ*, 882, 169, doi: [10.3847/1538-4357/ab3977](https://doi.org/10.3847/1538-4357/ab3977)
- Fernley, J., & Barnes, T. G. 1996, *A&A*, 312, 957
- For, B.-Q., Sneden, C., & Preston, G. W. 2011, *ApJS*, 197, 29, doi: [10.1088/0067-0049/197/2/29](https://doi.org/10.1088/0067-0049/197/2/29)
- Freeman, K. C., & Rodgers, A. W. 1975, *ApJL*, 201, L71, doi: [10.1086/181945](https://doi.org/10.1086/181945)
- Gillet, D., & Fokin, A. B. 2014, *A&A*, 565, A73, doi: [10.1051/0004-6361/201322938](https://doi.org/10.1051/0004-6361/201322938)
- Gillet, D., Sefyani, F. L., Benhida, A., et al. 2016, *A&A*, 587, A134, doi: [10.1051/0004-6361/201527287](https://doi.org/10.1051/0004-6361/201527287)
- Govea, J., Gomez, T., Preston, G. W., & Sneden, C. 2014, *ApJ*, 782, 59, doi: [10.1088/0004-637X/782/2/59](https://doi.org/10.1088/0004-637X/782/2/59)
- Gratton, R. G., Bragaglia, A., Clementini, G., et al. 2004, *A&A*, 421, 937, doi: [10.1051/0004-6361:20035840](https://doi.org/10.1051/0004-6361:20035840)
- Hansen, C. J., Nordström, B., Bonifacio, P., et al. 2011, *A&A*, 527, A65, doi: [10.1051/0004-6361/201015076](https://doi.org/10.1051/0004-6361/201015076)
- Jayasinghe, T., Kochanek, C. S., Stanek, K. Z., et al. 2018, *MNRAS*, 477, 3145, doi: [10.1093/mnras/sty838](https://doi.org/10.1093/mnras/sty838)
- Jayasinghe, T., Stanek, K. Z., Kochanek, C. S., et al. 2019, *MNRAS*, 485, 961, doi: [10.1093/mnras/stz444](https://doi.org/10.1093/mnras/stz444)
- Kock, M., Kroll, S., & Schnehage, S. 1984, *Physica Scripta Volume T*, 8, 84, doi: [10.1088/0031-8949/1984/T8/013](https://doi.org/10.1088/0031-8949/1984/T8/013)
- Lambert, D. L., Heath, J. E., Lemke, M., & Drake, J. 1996, *ApJS*, 103, 183, doi: [10.1086/192274](https://doi.org/10.1086/192274)
- Lancaster, L., Koposov, S. E., Belokurov, V., Evans, N. W., & Deason, A. J. 2019, *MNRAS*, 486, 378, doi: [10.1093/mnras/stz853](https://doi.org/10.1093/mnras/stz853)
- Layden, A. C. 1994, *AJ*, 108, 1016, doi: [10.1086/117132](https://doi.org/10.1086/117132)
- Layden, A. C., Hanson, R. B., Hawley, S. L., Klemola, A. R., & Hanley, C. J. 1996, *AJ*, 112, 2110, doi: [10.1086/118167](https://doi.org/10.1086/118167)
- Liu, G. C., Huang, Y., Zhang, H. W., et al. 2020, *ApJS*, 247, 68, doi: [10.3847/1538-4365/ab72f8](https://doi.org/10.3847/1538-4365/ab72f8)

- Liu, S., Zhao, G., Chen, Y.-Q., Takeda, Y., & Honda, S. 2013, *Research in Astronomy and Astrophysics*, 13, 1307, doi: [10.1088/1674-4527/13/11/003](https://doi.org/10.1088/1674-4527/13/11/003)
- Longmore, A. J., Fernley, J. A., & Jameson, R. F. 1986, *MNRAS*, 220, 279, doi: [10.1093/mnras/220.2.279](https://doi.org/10.1093/mnras/220.2.279)
- Magurno, D., Sneden, C., Braga, V. F., et al. 2018, *ApJ*, 864, 57, doi: [10.3847/1538-4357/aad4a3](https://doi.org/10.3847/1538-4357/aad4a3)
- Magurno, D., Sneden, C., Bono, G., et al. 2019, *ApJ*, 881, 104, doi: [10.3847/1538-4357/ab2e76](https://doi.org/10.3847/1538-4357/ab2e76)
- Marconi, M., Coppola, G., Bono, G., et al. 2015, *ApJ*, 808, 50, doi: [10.1088/0004-637X/808/1/50](https://doi.org/10.1088/0004-637X/808/1/50)
- May, M., Richter, J., & Wichelmann, J. 1974, *A&AS*, 18, 405
- Meléndez, J., & Barbuy, B. 2009, *A&A*, 497, 611, doi: [10.1051/0004-6361/200811508](https://doi.org/10.1051/0004-6361/200811508)
- Moore, C. E., Minnaert, M. G. J., & Houtgast, J. 1966, *The solar spectrum 2935 Å to 8770 Å*
- Nemec, J. M., Cohen, J. G., Ripepi, V., et al. 2013, *ApJ*, 773, 181, doi: [10.1088/0004-637X/773/2/181](https://doi.org/10.1088/0004-637X/773/2/181)
- Noguchi, K., Aoki, W., Kawanomoto, S., et al. 2002, *PASJ*, 54, 855, doi: [10.1093/pasj/54.6.855](https://doi.org/10.1093/pasj/54.6.855)
- O'Brian, T. R., Wickliffe, M. E., Lawler, J. E., Whaling, W., & Brault, J. W. 1991, *Journal of the Optical Society of America B Optical Physics*, 8, 1185, doi: [10.1364/JOSAB.8.001185](https://doi.org/10.1364/JOSAB.8.001185)
- Pancino, E., Britavskiy, N., Romano, D., et al. 2015, *MNRAS*, 447, 2404, doi: [10.1093/mnras/stu2616](https://doi.org/10.1093/mnras/stu2616)
- Pojmanski, G. 2002, *AcA*, 52, 397, <https://arxiv.org/abs/astro-ph/0210283>
- Preston, G. W. 1959, *ApJ*, 130, 507, doi: [10.1086/146743](https://doi.org/10.1086/146743)
- Ruffoni, M. P., Den Hartog, E. A., Lawler, J. E., et al. 2014, *MNRAS*, 441, 3127, doi: [10.1093/mnras/stu780](https://doi.org/10.1093/mnras/stu780)
- Saha, A. 1985, *ApJ*, 289, 310, doi: [10.1086/162890](https://doi.org/10.1086/162890)
- Sandage, A., & Tammann, G. A. 2006, *ARA&A*, 44, 93, doi: [10.1146/annurev.astro.43.072103.150612](https://doi.org/10.1146/annurev.astro.43.072103.150612)
- Sesar, B., Hernitschek, N., Mitrović, S., et al. 2017, *AJ*, 153, 204, doi: [10.3847/1538-3881/aa661b](https://doi.org/10.3847/1538-3881/aa661b)
- Shappee, B. J., Prieto, J. L., Grupe, D., et al. 2014, *ApJ*, 788, 48, doi: [10.1088/0004-637X/788/1/48](https://doi.org/10.1088/0004-637X/788/1/48)
- Sneden, C. 1973, *ApJ*, 184, 839, doi: [10.1086/152374](https://doi.org/10.1086/152374)
- Sneden, C., Preston, G. W., Chadid, M., & Adamów, M. 2017, *ApJ*, 848, 68, doi: [10.3847/1538-4357/aa8b10](https://doi.org/10.3847/1538-4357/aa8b10)
- Stringer, K. M., Long, J. P., Macri, L. M., et al. 2019, *AJ*, 158, 16, doi: [10.3847/1538-3881/ab1f46](https://doi.org/10.3847/1538-3881/ab1f46)
- Suntzeff, N. B., Kinman, T. D., & Kraft, R. P. 1991, *ApJ*, 367, 528, doi: [10.1086/169650](https://doi.org/10.1086/169650)
- Tody, D. 1993, in *Astronomical Society of the Pacific Conference Series*, Vol. 52, *Astronomical Data Analysis Software and Systems II*, ed. R. J. Hanisch, R. J. V. Brissenden, & J. Barnes, 173
- Torelli, M., Iannicola, G., Stetson, P. B., et al. 2019, *A&A*, 629, A53, doi: [10.1051/0004-6361/201935995](https://doi.org/10.1051/0004-6361/201935995)
- Torrealba, G., Catelan, M., Drake, A. J., et al. 2015, *MNRAS*, 446, 2251, doi: [10.1093/mnras/stu2274](https://doi.org/10.1093/mnras/stu2274)
- Wallerstein, G., Gomez, T., & Huang, W. 2012, *Ap&SS*, 341, 89, doi: [10.1007/s10509-012-1033-6](https://doi.org/10.1007/s10509-012-1033-6)
- Wallerstein, G., Kovtyukh, V. V., & Andrievsky, S. M. 2009, *ApJL*, 692, L127, doi: [10.1088/0004-637X/692/2/L127](https://doi.org/10.1088/0004-637X/692/2/L127)
- Weber, M., Granzer, T., & Strassmeier, K. G. 2012, in *Society of Photo-Optical Instrumentation Engineers (SPIE) Conference Series*, Vol. 8451, *Software and Cyberinfrastructure for Astronomy II*, 84510K, doi: [10.1117/12.926525](https://doi.org/10.1117/12.926525)
- Yanny, B., Rockosi, C., Newberg, H. J., et al. 2009, *AJ*, 137, 4377, doi: [10.1088/0004-6256/137/5/4377](https://doi.org/10.1088/0004-6256/137/5/4377)
- Zhao, G., Zhao, Y.-H., Chu, Y.-Q., Jing, Y.-P., & Deng, L.-C. 2012, *Research in Astronomy and Astrophysics*, 12, 723, doi: [10.1088/1674-4527/12/7/002](https://doi.org/10.1088/1674-4527/12/7/002)
- Zinn, R., & West, M. J. 1984, *ApJS*, 55, 45, doi: [10.1086/190947](https://doi.org/10.1086/190947)